DIGITALCOMMONS
@WAYNESTATE

Wayne State University

Wayne State University Dissertations

January 2022

Optical Signal Processing With Discrete-Space Metamaterials

Mohammad Moein Moeini
Wayne State University

Follow this and additional works at: https://digitalcommons.wayne.edu/oa_dissertations

 Part of the Electromagnetics and Photonics Commons, and the Optics Commons

Recommended Citation

Moeini, Mohammad Moein, "Optical Signal Processing With Discrete-Space Metamaterials" (2022). *Wayne State University Dissertations*. 3686.
https://digitalcommons.wayne.edu/oa_dissertations/3686

This Open Access Dissertation is brought to you for free and open access by DigitalCommons@WayneState. It has been accepted for inclusion in Wayne State University Dissertations by an authorized administrator of DigitalCommons@WayneState.

OPTICAL SIGNAL PROCESSING WITH DISCRETE-SPACE METAMATERIALS

by

MOHAMMAD MOEIN MOEINI

DISSERTATION

Submitted to the Graduate School,

of Wayne State University,

Detroit, Michigan

in partial fulfillment of the requirements

for the degree of

DOCTOR OF PHILOSOPHY

2022

MAJOR: Electrical Engineering

Approved By:

_____

Advisor Date

_____

_____

_____

_____

ACKNOWLEDGEMENTS

I take this opportunity to acknowledge and extend my sincere gratitude to my PhD supervisor Prof. Dimitrios L. Sounas for his wonderful leadership, endorsement upon my capabilities and endless support during this journey. I would like to thank committee members Prof. Ivan Avrutsky, Prof. Andrea Alu, Prof. Amar Basu and Prof. Gozde Tutuncuoglu for their constructive comments. Finally, I express my great appreciation to my family for their support and love.

TABLE OF CONTENTS

Acknowledgements ii

List of Tables v

List of Figures v

Chapter 1 Introduction 1

Chapter 2 Edge Detection 7

2.1 Sampling Array 7

2.2 Analysis of the Antenna Array 10

2.3 Subtracting Metamaterial 15

2.4 Analysis of the subtracting waveguide 18

2.5 Response Under Plane-wave Incidence 23

2.6 Photo-detection Integration and Numerical Aperture 27

Chapter 3 Optical Image Compression 30

Chapter 4 RGB to YUV All-optical Color Encoding 42

Chapter 5 High Impedance Matching Metamaterials with Topology Optimization . 48

Chapter A APPENDIX A 56

Appendix A 56

A.1 Calculation of the output signal of the full system 56

A.2 Lens Antenna Design 58

Chapter B APPENDIX B 61

Appendix B 61

B.1 Wavelet transform matrix 61

B.2 Output signals of the lenses 67

References 71

Abstract 79

Autobiographical Statement 80

LIST OF FIGURES

Figure 1 Discrete space optical signal processing. (a) Illustration of the concept. An array of optical antennas is used to sample an impinging optical field in space. Then, the desired operation is performed on the sampled field through a network with a discrete number of input/output ports. (b) Realistic implementation of the proposed concept. Top apertures are used to sample incoming wave profile. The sampled signals are supplied to a waveguide structure that realizes the desired mathematical operation. The composition of the waveguide may be complex, depending on the operation. Photodetectors collect the output waves at bottom openings. The lenses are used to increase the effective area of the apertures and enhance the efficiency of the system. 2

Figure 2 Design of the sampling antenna. (a) Optical fields are sampled in space through apertures on a metallic wall. The apertures are supplemented with a leaky-wave air cavity and a lens to enhance their affective area and consequently maximize the amount of collected power. (b) Radiation pattern of the lens-aperture system. (c) Electric field for excitation with a plane wave with incident angle $\theta = 0^\circ$ (left) and $\theta = 3^\circ$ (right). The dimensions of the structures have the following values: $L = 22\lambda$, $h_1 = 0.038\lambda$, $h_2 = 0.45\lambda$, $W = \lambda/(2\sin 3^\circ)$, where λ is the wavelength in free space. 8

Figure 3 A linear array of antennas excited by signals x_n. 10

Figure 4 Radiation pattern of the antenna with an angular range $-10^\circ < \theta < 10^\circ$ 15

Figure 5 Discrete port network for implementing a difference operation. (a) The network is based on a parallel-plate waveguide with periodic arrays of input/output channels at opposite walls. The collected signals from the antenna array are injected to the network through the top channels, while the processed signal is retrieved through the bottom ones. The difference operation is achieved by displacing the output channels compared to the input ones by an appropriately selected distance d. The obstacles in the vicinity of the T-junctions between the channels and the waveguide are added for matching purposes. The dimensions of the structure are as follows: $d = 0.477W$, $w_{\mathrm{g}} = 0.18\lambda$, $r = \frac{w_{\mathrm{g}}}{2} - 0.02\lambda_{\mathrm{g}}$ and $w_{\mathrm{o}} = 0.018\lambda_{\mathrm{g}}$ where λ_{g} is the guide wavelength inside the core waveguide. W is the same as for the sampling array in Fig. 2. (b) Transmission coefficient versus incident angle θ and frequency. The center frequency is $f_0 = 1.1f_{\mathrm{c}}$, where f_{c} is the cutoff frequency of the core waveguide. 16

Figure 6 Illustration of wave profiles coefficients inside the subtarctor metasurface waveguide. 20

Figure 7 Response of the full structure (antenna array and ensuing waveguide). (a) Intensity and phase of the transmission coefficient compared to ideal difference response. (b) Transmission versus frequency and illumination angle. 24

Figure 8 Response of the structure under illumination with a generic optical field. Three cases for the length of the input image are analyzed, 500λ, 700λ and 900λ, with the smallest length yielding an angular spectrum equal to the one of the structure. The results are derived for 5 different frequencies spanning the entire bandwidth of the structure. In all cases, the response is very close to the ideal difference response. . . . 27

Figure 9 Sensor array integration with OSP approaches. Nonlocal metasurfaces are designed with a large numerical aperture (NA=0.3); much larger than the desired NA for an array with periodicity of 0.5 μm. . . 28

Figure 10 Trade-off between radiation decay rate τ_{sw} and temporal frequency bandwidth BW. Strong nonlocality needs large radiation decay and therefore narrow bandwidth. Looking at two extreme cases of τ_{sw} may provide a better insight into this trade-off. An impulse τ_{sw} as a function of time excites infinite number of frequencies (very large BW) and a constant τ_{sw} over time results a single frequency radiation (very small BW). 29

Figure 11 Conceptual illustration of an optical implementation of the DWT transform. (a) An incident wave is discretized in space through an array of lenses. The discrete outputs of the array are guided to a network with a discrete number of input and output ports that implements the Haar matrix. The output wave of the network are guided to a photodetector array. The periodicity of the lens array is the same as the one of the photodetector array. (b) Three-dimensional artistic rendering of the concept. 32

Figure 12 Optical implementation of the one-dimensional Haar DWT transform of scale P for a system with 2^J pixels. The structure is a combination of 2^{J-P} identical networks each of which has 2^P input and 2^P output ports and a transformation matrix $\mathbf{H}_0$ equal to the Haar matrix. 34

Figure 13 Field distribution of combined lens array and Haar transformer metamaterials. Lens are individually excited by Gaussian beams of unitary power. 36

Figure 14 Constituent block of the optical implementation of the two-level Haar transform. (a) Structure of the block. (b) Simulation results for excitation with Gaussian beams for a different lens at a time. The bar diagrams compare the output power from simulations and from the ideal Haar matrix (Eq. (B.24)). (c) Simulation results for an incident wave modeling a 4-pixel image with a pixel vector $[1\,1\,-1\,-1]$. The bar diagram compares the power from simulations and the one calculated from the Haar matrix in Eq. (3.4) for an input vector calculated as the weighted average of the incident wave according to Eq. (3.3). (d) The same as (c), but for a sinusoidal incident wave representing a smoothened version of the same input image. 37

Figure 15 Operation of the optical implementation of the Haar transform on an image. (a) Input image. (b) Histogram of the input image. (c) Output image. (d) Histogram of the output image. The Haar transform is applied to the rows of the input image. 39

Figure 16 (a) Representation of chromatic dimensions of YUV color encoding model. V-U plane colorcode distribution changes with Y variation. Here, V-U is plotted at Y=0.5. (b) A sample image encoded in YUV model. Credit to Wikipedia 43

Figure 17 1 to 3 Gaussian beam to waveguide mode wavelength demultiplexer. Input Gaussian beams share the same beam opening with respect to λ. That is the reason the actual beam opening in the simulations look to have different lengths. Color Separation efficient for $1948nm$, $1648nm$ and $1500nm$ are $\%85$, $\%87$ and $\%87$, respectively. 45

Figure 18 RGB to YUV transformer metamaterial. Wavveguide modes at $1948nm$, $1648nm$ and $1500nm$ with unitary powers excite the metamaterial while outputs are optimized to converge to columns of matrix P at each wavelength. The metamaterial shows overall efficiency of $\%89$, $\%87$ and $\%90$ at each wavelength respectively. The binary material takes $\epsilon_r = 1$ and $\epsilon_r = 2.26$. 46

Figure 19 (a) Original image. (b) RGB representation. (c) Ideal YUV components. (d) Transformed YUV obtained from the inverse-designed metamaterial. 47

Figure 20 (a) Receiver front end of a conventional communication system. (b) Proposed idea to maximize high impedance matching with inverse-design metamaterials. 48

Figure 21 Circuit model of coaxial cable input impedance penetrating a parallel plate waveguide to harvest input power. The actual electric field has a non-zero value only along δ. Effective electric field used to make the connection between the physical and numerical model is and average electric field over the waveguide cross-section with length h. 51

Figure 22 FDFD discretization grid and TE field components arrangement. Lossy ϵ_{eff} is a fixed boundary condition only at point (i, k) while permittivty at other ponts of the grid go through inverse topology optimization with no impedance constraint. 52

Figure 23 Field, intensity and topology comparison of impedance matching metamaterial for loads $Z = 5k\Omega$ and $Z = 20k\Omega$. Topology optimization is performed for two sizes of optimization domain ($2.64\lambda_0$ and $1.17\lambda_0$) to illustrate fundamental limits. 53

Figure 24 Gaussian input to load impedance coupling efficiency vs dimensions of rectangular optimization domain. The study minimized a proper cost function for 3000 iterations or stops each loop upon reaching $\%90$ efficiency. 54

Figure 25 Left, middle and right lenses show ellptical configuration derived from Fermat's law, trancated lens and leaky-wave cavity embedded lens, respectively. 59

Figure 26 Lens design illustration. The dotted black and solid blue lines show the elliptical and extended hemispherical lenses, respectively. The orange dashed lines indicated the truncated region for the case of a periodic array. The solid red lines depict the radiated field. 59

Figure 27 Scaling and wavelet functions of the Haar transform for scales 0 to 2. 65

Figure 28 Contour around a lens for the application of the reciprocity theorem. . 68

CHAPTER 1 INTRODUCTION

Image processing is an essential part of modern technology, with a wide range of applications, such as in autonomous cars, medical devices, computer vision systems and augmented reality interfaces. An image processing system typically consists of two parts, an optical unit collecting impinging light and converting it to electrical signals and a digital one for processing the collected signals. The optical unit is usually a combination of lenses and photodetectors and it operates at very high speed, theoretically the speed of light, and with minimal power consumption. On the other hand, the digital unit is built up with billions of transistors, which consume power and have operation speed restrictions. Given that integrated circuits are quickly approaching the limits of Moore's law, it is clear that an all-digital approach can hardly meet the constantly increasing demands for smaller, faster and power-efficient devices. For this reason, the old field of optical signal processing (OSP) has recently attracted renewed attention [1, 2, 3]. Replacing all or some of the digital processing unit with an optical component utilizing only light to carry out the desired processing operation may allow to largely overcome some of the speed restrictions and power consumption problems of existing digital approaches. This paradigm has quickly gained traction and successfully been explored for applications in edge detection [4, 5, 6, 7, 8, 9, 10, 11, 12, 13, 14, 15, 16, 17], optimization [18, 19], machine learning [20, 21], pattern recognition [22, 23] and analog computation [24, 25].

Conventional OSP is based on Fourier optics and consists in converting an optical signal to Fourier space through lenses, performing the desired operation in the Fourier space through partially transparent screens or metasurfaces, and finally converting back to the

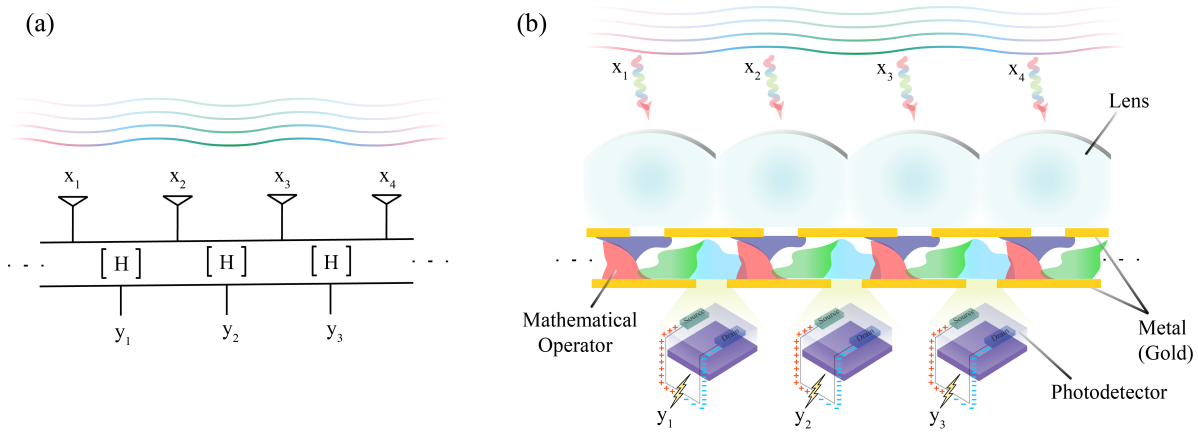

Figure 1: Discrete space optical signal processing. (a) Illustration of the concept. An array of optical antennas is used to sample an impinging optical field in space. Then, the desired operation is performed on the sampled field through a network with a discrete number of input/output ports. (b) Realistic implementation of the proposed concept. Top apertures are used to sample incoming wave profile. The sampled signals are supplied to a waveguide structure that realizes the desired mathematical operation. The composition of the waveguide may be complex, depending on the operation. Photodetectors collect the output waves at bottom openings. The lenses are used to increase the effective area of the apertures and enhance the efficiency of the system.

spatial domain through another set of lenses [26]. Despite its robustness and generality, this approach leads to bulky devices and therefore is not very attractive for modern systems. As a solution to this problem, several recent studies have explored metasurfaces, with the goal of tailoring their nonlocal response to the spatial Fourier transform of a desired operation. Such a task can for example be achieved through leaky wave resonances, taking advantage of their strong spatial dispersion [1, 6, 9, 13, 15, 16]. Another option is using the Brewster effect or geometrical phase, which leads to broadband responses, but with less flexibility over the realized nonlocal response [5, 7, 11, 8, 12, 14, 17]. Metasurface approaches have so far been limited to simple operations, like differentiation or integration, most likely because they rely on physical mechanisms with specific nonlocal responses that are difficult to be matched to complex mathematical operations. Further-

more, since they often depend on resonant effects, they are subject to limitations in terms of bandwidth versus nonlocality, imposing another restriction on the responses that can be achieved.

This thesis introduces a radically new approach to OSP, with the ability to implement general mathematical operations without the limitations of other approaches. To this end we borrow inspiration from digital filters, where a signal is first discretized in time, then the desired operation is performed in the digital domain and finally the output signal is converted back to the analog domain [27]. Following this paradigm, we propose a system where an optical signal is sampled in space through an array of antennas and subsequently supplied to a nano-photonic network with a discrete number of input and output ports that performs the desired mathematical operation (Fig. 1a). The output of this network is a discrete signal in space and can be directly supplied to an array of photodetectors, thus saving us from having to convert the signal back to the analog domain, as in conventional digital filters. Similar to digital filters, our system offers great versatility for implementing general operations, since its design boils down to the design of a discrete port network with a given scattering matrix, which, as has been recently shown, can be efficiently executed through inverse design algorithms [28]. We demonstrate the proposed paradigm for the case of edge detection (differentiation) and the novel concepts of image compression and color encoding transformation (in chapters 2, 3 and 4, respectively) via a structure consisting of an array of lens antennas for sampling the signal in space and a waveguide with periodic arrays of input and output apertures for implementing the desired mathematical operation.

The proposed discrete-space design approach has significant advantages compared to

the currently main approach for OSP based on momentum-domain metasurfaces. First, since we do not rely on momentum domain design characteristics, such as leaky-wave resonances, we design metamaterials with a relatively large bandwidth. For example, in the case of edge detection the proposed design supports a 5% frequency bandwidth, which is one of the largest reported in the literature. Second, direct spatial design is not subject to the restrictions of the physical effects used in momentum-based approaches, like leaky-wave resonances, and unveils a way to implement a variety of mathematical operations. In other words, as long as the design expectations are not against fundamental electromagnetic principles, like power conservation and reciprocity, one can design any scattering matrix. This flexibility of the discrete space approach has allowed us to propose for the first time image compression in the optical domain through a structure that implements the Haar wavelet transform, which is one of the mathematical operations used in the JPEG image compression algorithm. The fairly complex nature of this transform makes its implementation through a momentum-based metasurface a rather challenging, if not impossible, task. On the other hand, with the discrete-space approach it turns out to the design of a linear network with a discrete number of input and output ports, which can be efficiently accomplished trough topology optimization. In our work, this task is accomplished through an in-house-developed Finite-Difference Frequency Domain (FDFD) inverse topology optimization algorithm.

Another problem of highly practical significance that was tackled in this thesis is color encoding (chapter 4). We targeted a transformation between two of the most well-known color codes, RGB and YUV. RGB represents light illumination based on color elements Red (R), Green (G) and Blue (B) only, while YUV separates intensity and color components

of light. Y represents intensity information, while color information is encoded in U and V. YUV has huge potential in communication engineering, image and video processing, bandwidth reduction, differential color representation and unique brittleness control capability. We obtain a proper scattering matrix to realize this transformation after a slight manipulation ta make sure the matrix satisfies conservation of power. Once again, combining discrete-space metamaterials and inverse design, we carefully optimized needed metamaterial to make the operation possible.

In chapter 5, we focus on a related problem problem in antenna engineering. Conventional communication systems are composed of an antenna and a Low Noise Amplifier (LNA) at the receiving end. However, large input impedance of the LNA often causes a considerable amount of power reflection between this two blocks, and therefore, enforces efficiency reduction over the entire receiving mechanism. Another case where impedance mismatch can be a serious problem is in energy harvesting systems, which are terminated to diodes with very high impedances, much different that the impedances of antennas. The conventional way for addressing these problems is by adding a matching network between the antenna and the load, but it is known that the efficiency of such networks drops quickly as the ratio between the input and output impedances increases. At the same time, there it no reason, at least at first sight, why an antenna cannot be design to have an impedance that matches the load impedance, which would render the matching network unnecessary. Here we try to address this possibility by exploring any fundamental trade-offs between the impedance of an antenna, and its efficiency and size. We tackle this problem by using the topology-optimization algorithm we have developed earlier in the thesis. We show that the an inverse-designed metamaterial antenna can convert an

incident beam to a high-impedance output signal with high efficiency, as long as the size of the antenna is beyond a limit determined by the value of the output impedance. The analysis reveals a previously unexplored trade-off for antennas and can be important for the design of wireless systems.

In summary, the discrete space approach introduced in this thesis constitutes a significant leap forward in the implementation of complex image processing operation with waves that cannot be achieved with other approaches. This fact is demonstrated for the practically important cases of edge detection, image compression and YUV color encoding. Furthermore, it is shown how the techniques developed in the thesis can be useful for understanding other important problems in antenna design. The discrete space approach is characteristic for its generality and capability to be integrated in imaging systems. As such, it has the potential of enabling a new class of smart cameras with high speed and ultra-low power consumption.

CHAPTER 2 EDGE DETECTION

2.1 Sampling Array

A simple way to realize sampling in space is through a periodic array of apertures on a metallic layer, as in Fig. 1b. According to the Nyquist-Shannon theorem, the array periodicity needs to be selected as $W \leq \pi/k_{\mathrm{t,max}}$, where $k_{\mathrm{t,max}}$, is the maximum transverse wavenumber of the impinging optical signal, which is the analogue of angular frequency in the spatial domain. Any value below this limit is permitted, but, as will become clear later, operating exactly on the limit leads to the simplest form for the spatial filter. Apertures on a metallic layer are effective magnetic dipoles with an effective aperture approximately equal to $\lambda/2$, λ being the wavelength in free space [29]. Since $k_{\mathrm{t,max}} < k$, where k is the wavenumber in free space, we find from $W = \pi/k_{\mathrm{t,max}}$ that $W > \lambda/2$, meaning that the apertures can only capture a fraction of the impinging power, limiting the system's efficiency. An array of lenses on top of the apertures solves this problem and improves the efficiency of the whole structure. Using Fermmat's principle, it can be shown that an ellipsoidal lens focuses a bundle of normally incident rays to one of the ellipse's focal points [30]. Keeping this fact in mind, we position the openings at the lenses' focal points. A quarter-wavelength coating layer of relative permittivity $\epsilon_{\mathrm{coat}} = \sqrt{\epsilon_{\mathrm{lens}}}$, where ϵ_{lens} is the relative permittivity of the lens, is also added on the surface of the lens to eliminate air-lens impedance mismatch and multiple internal reflections. When the lenses are introduced in the periodic aperture array, they have to be truncated to a width matching the array periodicity. This leads to spillover loss and reduction of the power captured by the apertures. This fact can be better understood by examining the apertures in the

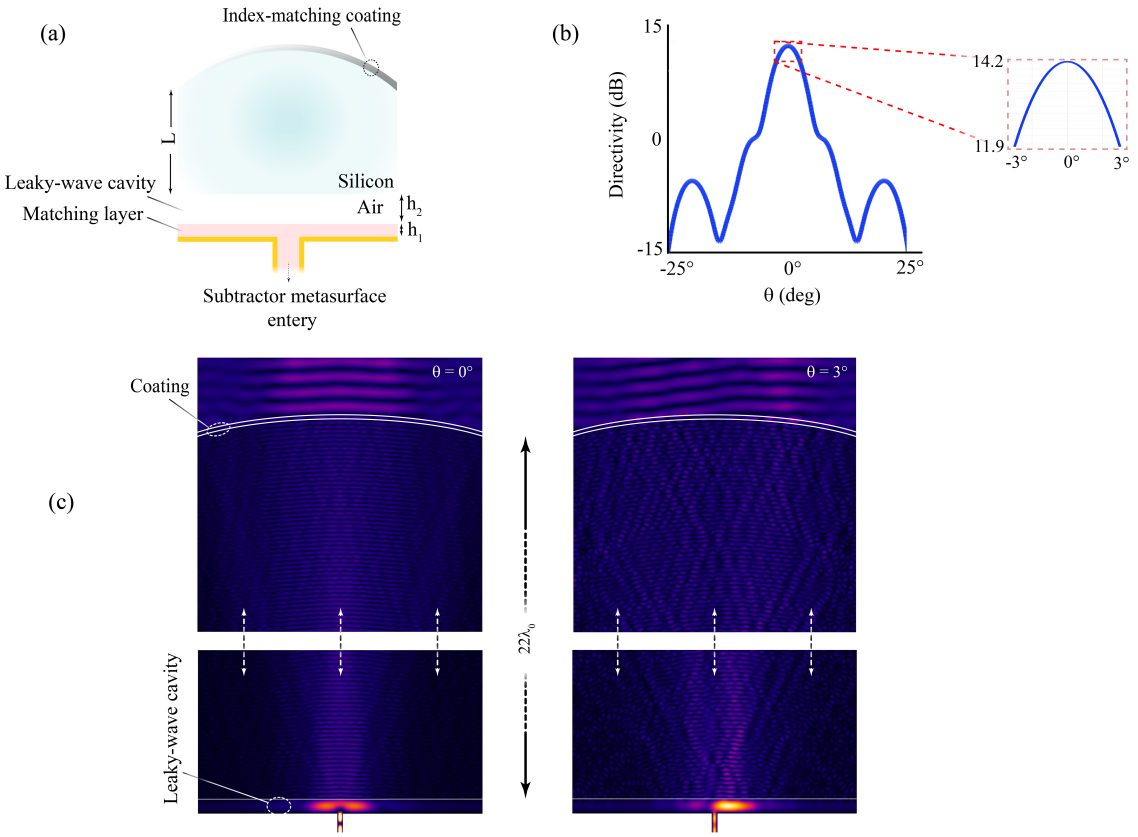

Figure 2: Design of the sampling antenna. (a) Optical fields are sampled in space through apertures on a metallic wall. The apertures are supplemented with a leaky-wave air cavity and a lens to enhance their affective area and consequently maximize the amount of collected power. (b) Radiation pattern of the lens-aperture system. (c) Electric field for excitation with a plane wave with incident angle $\theta = 0°$ (left) and $\theta = 3°$ (right). The dimensions of the structures have the following values: $L = 22\lambda$, $h_1 = 0.038\lambda$, $h_2 = 0.45\lambda$, $W = \lambda/(2\sin 3°)$, where λ is the wavelength in free space.

transmitting mode and taking into account that due to the reciprocity theorem the radiation pattern is identical in the receiving and transmitting modes. When the apertures are operated as transmitters, the lenses capture only a portion of the radiated power, in particular the one inside the cones defined by the apertures and the lenses, thus limiting the radiated power and consequently the effective area towards the normal direction. To overcome this problem, we have added a low-index (here air) dielectric slab with a height of approximately half a wavelength between the aperture and the lens, designed to sup-

port a broadband leaky-wave resonance with the ability to focus the radiated power from the aperture within the aperture-lens cone [31, 32]. From reciprocity, it directly follows that such a strategy also increases the receiving efficiency of the apertures.

Based on the above remarks, we have designed a two-dimensional antenna as in Fig. 2a, assuming an out-of-plane (transverse-electric (TE)) electric field polarization. The lens is made of a material with a relative permittivity $\epsilon_{\text{lens}} = 9$ and approximated as a spherical sector. The apertures are connected to short channels in the metallic layer with the same width as the apertures, to guide the received signals to the processing part of the system. The channels are filled with a dielectric material $\varepsilon_{\text{r}} = 9$. In order to avoid impedance mismatch between the leaky-wave air cavity and the channels, we slightly extend the dielectric material of the channels to the top of the aperture array. The system is designed for optical fields with angular spread from -3° to 3°, which corresponds to $k_{\text{t,max}} = k \sin\theta_{\text{max}}$, where $\theta_{\text{max}} = 3^\circ$. This value was selected so that at 600 nm (approximately the middle of the optical spectrum), $W = 5.7$ μm, which is a typical pixel size in commercial imaging systems. Ideally, we would like the radiation pattern to be flat for $-\theta_{\text{max}} < \theta < \theta_{\text{max}}$ with effective aperture equal to W and 0 otherwise. In reality, the radiation pattern is smoother, as in Fig. 2b. Then, θ_{max} is the cutoff angle of the structure, at which directivity drops by 3 dB compared to its value at $\theta = 0^\circ$. Fig. 2b shows the simulation results of the electric field intensity for $\theta = 0^\circ$ and $\theta = 3^\circ$. For both illumination angles, the extended hemispherical lens and the index-matching layer focus the incoming waves on the leaky wave cavity. Although the focal point for $\theta = 3^\circ$ excitation is slightly shifted off to the right from the aperture, the leaky-wave cavity helps the wave to couple to the waveguide thus mitigating this misalignment effect. By dividing the collected power in the channels by the incident

power over a single period W, we find that the effective area is $0.85W$ and $0.5W$ at $\theta = 0^\circ$ and $\theta = 3^\circ$, respectively.

2.2 Analysis of the Antenna Array

Here, we are going to analyze the response of the periodic antenna array to an impinging plane wave. As a first step, we will derive a general expression for the radiated field by a periodic antenna array. The problem of calculating the received power for excitation with a plane wave can be obtained from this result by applying reciprocity.

Fig. 3 shows a linear array of N antennas, with a periodicity W and input signals $x_n = x_0 e^{-jn\varphi}$, where φ is the phase difference between two adjacent antennas of the array. The problem is assumed two dimensional, i.e., uniform along the z-axis, with an electric field polarized along the z-axis, as the antennas in the main text. Consider, first, a single element of the array. The radiated field is given by

$$E(r,\theta) = x_{\text{in}} F(\theta) \frac{e^{-jkr}}{\sqrt{2\pi r}}, \tag{2.1}$$

where x_{in} is an input signal at the port of the antenna, $F(\theta)$ is the radiation pattern, k is

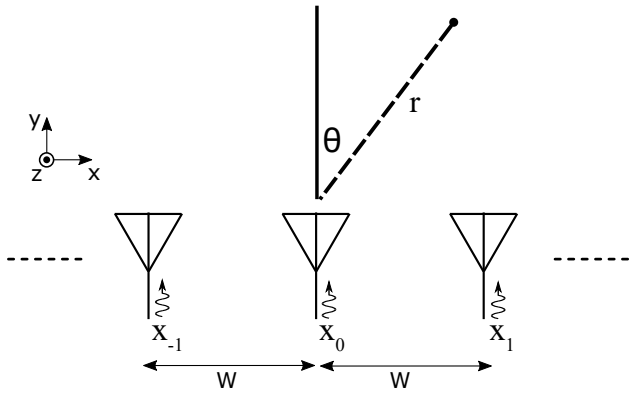

Figure 3: A linear array of antennas excited by signals x_n.

the wavenumber in free space, θ is the azimuthal angle defined as in Fig. 3 and r is the radial distance from the center of the antenna. The directivity is defined as

$$D(\theta) = \frac{U_{\mathrm{rad}}(\theta)}{U_{\mathrm{iso}}}, \tag{2.2}$$

where $U_{\mathrm{rad}}(\theta)$ is the radiation intensity of the antenna, i.e., the radiated power per unit angle, and U_{iso} is the radiated intensity of an isotropic antenna with the same radiated power. The radiation intensity of the antenna is given by

$$U_{\mathrm{rad}}(\theta) = r\frac{|E(r,\theta)|^2}{2\eta} = \frac{|x_{\mathrm{in}}|^2}{4\pi\eta}|F(\theta)|^2, \tag{2.3}$$

where η is the wave impedance in free space. The radiation intensity of the isotropic antenna is given by $U_{\mathrm{iso}} = P_{\mathrm{rad}}/(2\pi)$, where P_{rad} is the radiated power, which is equal to $P_{\mathrm{rad}} = |x_{\mathrm{in}}|^2/(2Z_{\mathrm{ant}})$, where Z_{ant} is the input impedance at the port of the antenna. Replacing these equations into (2.2) yields

$$D(\theta) = \frac{Z_{\mathrm{ant}}}{\eta}|F(\theta)|^2. \tag{2.4}$$

Furthermore, from (2.3) we have

$$U_{\mathrm{rad}}(\theta) = \frac{P_{\mathrm{rad}}}{2\pi}D(\theta). \tag{2.5}$$

Now, let us move to the case of the array. Following the antenna theory [33], the

radiated field by the array is given by

$$E(r,\theta) = x_0 AF(\theta)F(\theta)\frac{e^{-jkr}}{\sqrt{2\pi r}}, \tag{2.6}$$

where $AF(\theta)$ is the array factor given by

$$AF(\theta) = \sum_{n=-\frac{N}{2}}^{\frac{N}{2}-1} e^{-jn\psi} = e^{j\frac{\psi}{2}}\frac{\sin\left(\frac{N\psi}{2}\right)}{\sin\left(\frac{\psi}{2}\right)}, \tag{2.7}$$

where $\psi = \varphi - kW\sin\theta$. The radiation intensity is given by

$$U_{\text{rad}}(\theta) = r\frac{|E(r,\theta)|^2}{2\eta} = \frac{|x_0|^2}{4\pi\eta}|AF(\theta)|^2|F(\theta)|^2. \tag{2.8}$$

Replacing $|F(\theta)|^2$ from (2.4) into (2.8) results in

$$U_{\text{rad}}(\theta) = \frac{P_{\text{in}}}{2\pi}|AF(\theta)|^2 D(\theta), \tag{2.9}$$

where P_{in} is the input power at the port of each antenna in the array. Replacing (2.7) into (2.9) yields

$$U_{\text{rad}}(\theta) = \frac{P_{\text{in}}}{2\pi}\frac{\sin^2\left(\frac{N\psi}{2}\right)}{\sin^2\left(\frac{\psi}{2}\right)}D(\theta). \tag{2.10}$$

The total radiated power can be found through integration with respect to θ as

$$P_{\text{rad}} = \int_{-\pi}^{\pi} U_{\text{rad}}(\theta)d\theta = \frac{P_{\text{in}}}{2\pi}\int_{-\pi}^{\pi}\frac{\sin^2\left(\frac{N\psi}{2}\right)}{\sin^2\left(\frac{\psi}{2}\right)}D(\theta)d\theta. \tag{2.11}$$

If we assume antennas radiating only in the top-half space, i.e., for $-\pi/2 < \theta < \pi/2$, (2.11)

becomes

$$P_{\text{rad}} = \frac{P_{\text{in}}}{2\pi} \int_{-\frac{\pi}{2}}^{\frac{\pi}{2}} \frac{\sin^2\left(\frac{N\psi}{2}\right)}{\sin^2\left(\frac{\psi}{2}\right)} D(\theta) d\theta. \tag{2.12}$$

From the theory of distributions (Fejer's theorem) [34], it is known that

$$\lim_{N\to\infty} \frac{1}{N} \int_{-\pi}^{\pi} \left[\frac{\sin\left(\frac{Nx}{2}\right)}{\sin\left(\frac{x}{2}\right)}\right]^2 f(x)dx = 2\pi f(0), \tag{2.13}$$

where $f(x)$ is a continuous function in $(-\pi, \pi)$. This identity can be extended over an infinite range as follows

$$\lim_{N\to\infty} \frac{1}{N} \int_{-\infty}^{\infty} \left[\frac{\sin\left(\frac{Nx}{2}\right)}{\sin\left(\frac{x}{2}\right)}\right]^2 f(x)dx = 2\pi \sum_{m=-\infty}^{\infty} f(2m\pi). \tag{2.14}$$

(2.14) can be used to calculate the radiated power from each antenna element in the limit of an infinity array, which is defined by

$$P_{\text{ant}} = \lim_{N\to\infty} \frac{P_{\text{rad}}}{N}. \tag{2.15}$$

Specifically, changing the variable of integration from θ to ψ in (2.12) leads to

$$P_{\text{rad}} = \frac{P_{\text{in}}}{2\pi} \frac{1}{kW} \int_{\varphi-kW}^{\varphi+kW} \frac{\sin^2\left(\frac{N\psi}{2}\right)}{\sin^2\left(\frac{\psi}{2}\right)} \frac{D(\theta)}{\cos\theta} d\psi. \tag{2.16}$$

Replacing (2.16) into (2.15) and then applying (2.14) yields

$$P_{\text{ant}} = \frac{P_{\text{in}}}{kW} \sum_{m} \frac{D(\theta_m)}{\cos\theta_m}, \tag{2.17}$$

where θ_m are the solutions of the equation $\varphi - kW\sin\theta_m = 2m\pi$ in the range $(-\pi/2, \pi/2)$. Each term of the sum in (2.17) corresponds to a plane wave propagating along the angle θ_m with a total power $\frac{P_{\text{in}}}{kW}\frac{D(\theta_m)}{\cos\theta_m}$ within one unit cell. Therefore, the radiation efficiency of the antenna array along an angle θ is equal to $\frac{1}{kW}\frac{D(\theta_m)}{\cos\theta_m}$. Due to reciprocity, this equation also provides the receiving efficiency for an incident plane wave from the same angle

$$T_{\text{array}} = \frac{1}{kW}\frac{D(\theta)}{\cos\theta} \tag{2.18}$$

The received power is given by

$$P_{\text{rec}} = \frac{P_{\text{inc}}}{kW}\frac{D(\theta)}{\cos\theta}, \tag{2.19}$$

where P_{inc} is the incident power within one unit cell.

In order to have perfect collection of the incident power by the antenna array, it is necessary that $P_{\text{rec}} = P_{\text{inc}}$, leading to

$$D(\theta) = kW\cos\theta. \tag{2.20}$$

Furthermore, from the antenna theory, the directivity should satisfy

$$\int_{-\pi}^{\pi} D(\theta)d\theta = 2\pi. \tag{2.21}$$

It is not difficult to show that (2.20) and (2.21) are concurrently satisfied for an antenna

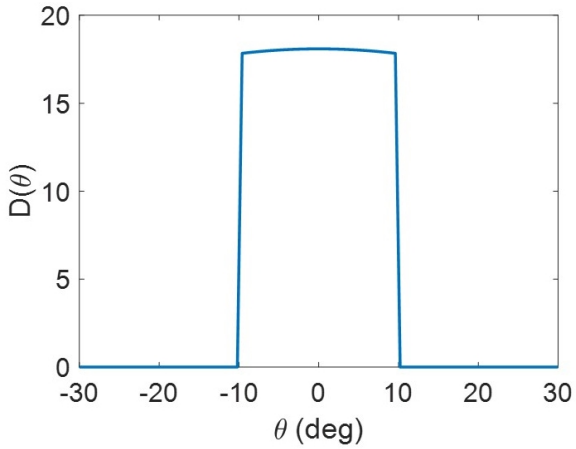

Figure 4: Radiation pattern of the antenna with an angular range $-10^\circ < \theta < 10^\circ$

with

$$D(\theta) = \begin{cases} kW\cos\theta, & -\theta_{\max} < \theta < \theta_{\max} \\ 0, & \text{otherwise} \end{cases}, \tag{2.22}$$

where $kW\sin\theta_{\max} = \pi$, which is the Nyquist-Shannon sampling condition of the array. Therefore, by satisfying the condition in (2.22), we can make sure that incident optical fields with an angular range from $-\theta_{\max}$ to $\theta_{\max}$ are perfectly captured by the array. Here, for instance, radiation directivity when $\theta_{max} = 10^\circ$ is plotted in Fig. 4.

2.3 Subtracting Metamaterial

The second part of the system is a linear optical network performing the desired mathematical operation. Here, this network is a waveguide formed between two metallic walls with an arbitrary material composition depending on the operation that has to be realized, as shown in Fig. 1b. The waveguide is connected to the antenna array through short channels on its top wall, from where the antenna signals x_n are injected. On the bottom wall of the waveguide there is another array of channels, from where the output signals y_n are

collected. Both arrays have the same periodicity W. Similar to digital filters, the output signals are given by an expression of the form

$$y_n = \sum_{k=-M}^{N} h_k x_{n-k}, \tag{2.23}$$

where M, N are integers and h_k is the impulse response of the structure. (2.23) states that the output signal at the n-th output aperture is a linear superposition of $M + N$ signals over the top apertures, essentially providing the scattering matrix of the network. Since we

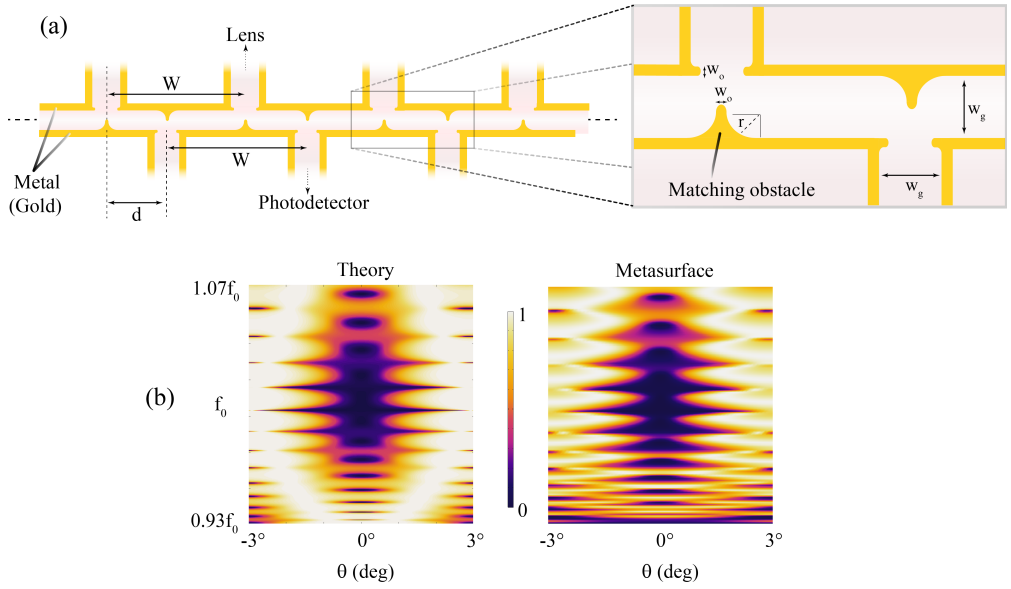

Figure 5: Discrete port network for implementing a difference operation. (a) The network is based on a parallel-plate waveguide with periodic arrays of input/output channels at opposite walls. The collected signals from the antenna array are injected to the network through the top channels, while the processed signal is retrieved through the bottom ones. The difference operation is achieved by displacing the output channels compared to the input ones by an appropriately selected distance d. The obstacles in the vicinity of the T-junctions between the channels and the waveguide are added for matching purposes. The dimensions of the structure are as follows: $d = 0.477W$, $w_{\rm g} = 0.18\lambda$, $r = \frac{w_{\rm g}}{2} - 0.02\lambda_{\rm g}$ and $w_{\rm o} = 0.018\lambda_{\rm g}$ where $\lambda_{\rm g}$ is the guide wavelength inside the core waveguide. W is the same as for the sampling array in Fig. 2. (b) Transmission coefficient versus incident angle θ and frequency. The center frequency is $f_0 = 1.1f_{\rm c}$, where $f_{\rm c}$ is the cutoff frequency of the core waveguide.

are dealing with signals in space, we are not limited by causality, hence the bottom limit in (2.23) can be a negative number. Quite importantly, (2.23) describes a translationally symmetric structure, as required to make sure that the response is insensitive to the lateral location of the incident signal with respect to the structure.

Taking into account the above remarks, we have designed a system performing a discrete derivative, i.e., difference, operation $y_n = x_{n+1} - x_n$. To this end, we use a waveguide filled with a uniform dielectric material $\epsilon_{\mathrm{r}} = 9$, which is the same material as for the input/output channels, and output channels displaced by a distance d with respect to the input ones, as shown in Fig. 5a. Assuming a nearest neighbor approximation, the signal at the n-th output channel is approximately equal to

$$y_n \approx \frac{1}{2} x_{n+1} e^{-j\beta(W-d)} + \frac{1}{2} x_n e^{-j\beta W}, \tag{2.24}$$

where β is the wavenumber inside the waveguide and the $\frac{1}{2}$ factor is due to the fact that the input signals are split to two parts propagating in opposite directions when they enter the waveguide. If d is selected such that $\beta(W - 2d) = (2m + 1)\pi$, where m is an integer, the output signal becomes

$$y_n \approx e^{-j\beta(W-d)}(x_{n+1} - x_n), \tag{2.25}$$

yielding the desired difference operation. From all possible values for d, we select the one that is closer to $W/2$, because, as will be shown later, it leads to maximum bandwidth. In order to eliminate reflections at the T-junctions between the input/output channels and the waveguide, we have added carefully designed metallic obstacles in the vicinity of the

junctions as shown in Fig. 5a, following the technique in [35].

2.4 Analysis of the subtracting waveguide

Here, we are going to analyze the transmission response of the core waveguide. Recall that the input channels of this waveguide carry the collected signals by the preceding antenna array. If the input/output channels are matched to the core waveguide, the scattering matrix of the T-junctions assumes the general form

$$\bar{\bar{S}} = \begin{bmatrix} 0 & \frac{1}{\sqrt{2}} & \frac{1}{\sqrt{2}} \\ \frac{1}{\sqrt{2}} & r & t \\ \frac{1}{\sqrt{2}} & t & r \end{bmatrix}, \tag{2.26}$$

where ports are defined as in Fig. 6, r is the reflection coefficient from port 2 or 3 and t is the transmission coefficient from port 2 to 3 or vice versa. The $1/\sqrt{2}$ terms originate from the fact that the incident signal from input channels is split to two equal parts propagating in opposite directions. Assuming a lossless network, we have

$$\bar{\bar{S}}^{\dagger}\bar{\bar{S}} = \bar{\bar{I}}, \tag{2.27}$$

where $\bar{\bar{I}}$ is the identity matrix and † represents the conjugate transpose operation. Inserting (2.26) into (2.27) results in

$$r + t = 0, \tag{2.28}$$

$$|r|^2 + |t|^2 = \frac{1}{2}. \tag{2.29}$$

(2.28) and (2.29) are satisfied for

$$r = -t = -\frac{1}{2}. \tag{2.30}$$

If the waves in the waveguide are defined as in Fig. 6, applying (2.26) to the left T-junction results in the following equations

$$A_2 = \frac{1}{\sqrt{2}} + tA_1 + rB_2, \tag{2.31}$$

$$B_1 = \frac{1}{\sqrt{2}} + tB_2 + rA_1. \tag{2.32}$$

Similarly, from the right junction we have

$$A_3 e^{j\beta(W-d)} = tA_2 e^{-j\beta d} + rB_3 e^{-j\beta(W-d)}, \tag{2.33}$$

$$B_2 e^{j\beta d} = rA_2 e^{-j\beta d} + tB_3 e^{-j\beta(W-d)}, \tag{2.34}$$

where β is the wavenumber in the waveguide. Assuming a plane-wave excitation with transverse wavenumber k_{t}, the signals at the input channels of the waveguide are of the form $x_n = x_0 e^{-jnk_{\mathrm{t}}}$, where x_n is the input signal at the n-th channel. As a result, at the boundaries of a unit cell of the waveguide defined between two consecutive input channels, as in Fig. 6, the fields satisfy the Floquet conditions

$$A_3 = A_1 e^{-j\varphi}, \tag{2.35}$$

$$B_3 = B_1 e^{-j\varphi}, \tag{2.36}$$

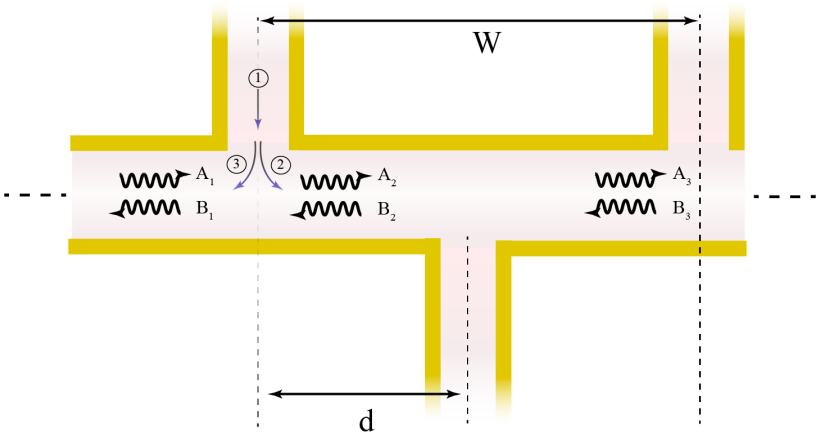

Figure 6: Illustration of wave profiles coefficients inside the subtarctor metasurface waveguide.

where $\varphi = k_{\mathrm{t}} W$. Solving (2.31)-(2.36) for A_2, B_3 and using $t = -r$ yields

$$A_2 = \frac{1}{\sqrt{2}} \frac{1 - 2r^2 \left[e^{-j(\varphi + \beta W)} + e^{-j2\beta(W-d)} \right]}{\Delta}, \tag{2.37}$$

$$B_3 = \frac{1}{\sqrt{2}} \frac{1 - 2r^2 \left[e^{j(\varphi - \beta W)} + e^{-j2\beta d} \right]}{\Delta} e^{-j\varphi}, \tag{2.38}$$

where

$$\Delta = 1 - 2r^2 \left\{ \cos\varphi + \cos[\beta(W - 2d)] \right\} e^{-j\beta W}. \tag{2.39}$$

The outgoing field at the output channel is given by

$$E_{\mathrm{out}} = \frac{1}{\sqrt{2}} \left[A_2 e^{-j\beta d} + B_3 e^{-j\beta(W-d)} \right]. \tag{2.40}$$

By inserting (2.37), (2.38) into (2.40) we find

$$E_{\mathrm{out}} = \frac{1}{\Delta} \left\{ e^{-j\frac{\varphi + \beta W}{2}} \cos\left[\frac{\varphi + \beta(W - 2d)}{2} \right] - 4r^2 e^{-j\frac{\varphi + 3\beta W}{2}} \cos\left[\frac{\varphi - \beta(W - 2d)}{2} \right] \right\}. \tag{2.41}$$

Replacing $r = -1/2$ into (2.41) leads to

$$E_{\text{out}} = \frac{1}{\Delta} e^{-j\frac{\varphi+2\beta W}{2}} \left\{ e^{j\frac{\beta W}{2}} \cos\left[\frac{\varphi+\beta(W-2d)}{2}\right] - e^{-j\frac{\beta W}{2}} \cos\left[\frac{\varphi-\beta(W-2d)}{2}\right] \right\}, \quad (2.42)$$

where

$$\Delta = 1 - \frac{1}{2}\left\{\cos\varphi + \cos\left[\beta(W-2d)\right]\right\} e^{-j\beta W}. \quad (2.43)$$

Considering that in the above analysis the incident field was assumed equal to 1, the transmission coefficient is found as

$$T_{\text{wg}} = |E_{\text{out}}|^2 = \frac{\left| e^{j\frac{\beta W}{2}} \cos\left[\frac{\varphi+\beta(W-2d)}{2}\right] - e^{-j\frac{\beta W}{2}} \cos\left[\frac{\varphi-\beta(W-2d)}{2}\right] \right|^2}{|\Delta|^2}. \quad (2.44)$$

Assume now that $\beta(W-2d) = (2m+1)\pi$, which is the condition for obtaining a perfect difference operator. Then, (2.42) becomes

$$E_{\text{out}} = \mp \frac{2}{\Delta} e^{-j\frac{\varphi+2\beta W}{2}} \cos\left(\frac{\beta W}{2}\right) \sin\left(\frac{\varphi}{2}\right), \quad (2.45)$$

where the minus/plus sign hold for even/odd m. The output field in (2.45) is proportional to $\sin(\varphi/2)$, which represents a difference operator in the Fourier space.

If we analyze the sinusoidal functions in (2.41) to complex exponentials and multiply both sides of the equation with 2Δ we get

$$\begin{aligned} &2\left\{1 - 2r^2\cos\left[\beta(W-2d)\right] e^{-j\beta W}\right\} E_{\text{out}} - 2r^2 e^{-j\beta W} e^{j\varphi} E_{\text{out}} - 2r^2 e^{-j\beta W} e^{-j\varphi} E_{\text{out}} \\ &= \left[e^{-j\beta d} - 4r^2 e^{-j\beta(2W-d)}\right] + \left[e^{-j\beta(W-d)} - 4r^2 e^{-j\beta(W+d)}\right] e^{-j\varphi}. \end{aligned} \quad (2.46)$$

Taking into account that the incident field from channel $n = 0$ is equal to 1, we can write $x_0 = 1$ and $x_1 = e^{-j\varphi}$. Similarly, $y_0 = E_{\text{out}}$, $y_{-1} = e^{j\varphi}E_{\text{out}}$ and $y_1 = e^{-j\varphi}E_{\text{out}}$. Then, (2.46) becomes

$$\begin{aligned} &2\left\{1 - 2r^2\cos\left[\beta(W-2d)\right]e^{-j\beta W}\right\}y_0 - 2r^2e^{-j\beta W}y_{-1} - 2r^2e^{-j\beta W}y_1 \\ &= \left[e^{-j\beta d} - 4r^2e^{-j\beta(2W-d)}\right]x_0 + \left[e^{-j\beta(W-d)} - 4r^2e^{-j\beta(W+d)}\right]x_1. \end{aligned} \tag{2.47}$$

Since the structure is translationally symmetric, (2.47) can be written in the general form

$$\begin{aligned} &2\left\{1 - 2r^2\cos\left[\beta(W-2d)\right]e^{-j\beta W}\right\}y_n - 2r^2e^{-j\beta W}y_{n-1} - 2r^2e^{-j\beta W}y_{n+1} \\ &= \left[e^{-j\beta d} - 4r^2e^{-j\beta(2W-d)}\right]x_n + \left[e^{-j\beta(W-d)} - 4r^2e^{-j\beta(W+d)}\right]x_{n+1}. \end{aligned} \tag{2.48}$$

If $r = 0$, i.e., the waves in the waveguide were not reflected by the T-junctions, (2.48) would take the form

$$2e^{-j\beta W}y_n = e^{-j\beta d}x_n + e^{-j\beta(W-d)}x_{n+1}, \tag{2.49}$$

which is Eq. (2) in the main text, derived under a nearest-neighbor assumption. In the more general case of $r \neq 0$, (2.48) shows that the output signal is the result of two contributions: 1) the input signals x_n, x_{n+1} from the nearest-neighbor input channels propagating towards the output channel (terms $e^{-j\beta d}$ and $e^{-j\beta(W-d)}$) and 2) reflections of these signals to each other's T-junction. For example, $e^{-j\beta(2W-d)}x_n$ is the input signal from channel n reaching the output channel n after being reflected at the T-junction of the input channel $n+1$. Similarly, $e^{-j\beta(W+d)}x_{n+1}$ is the the input signal from channel $n+1$ reaching the output channel n after being reflected at the T-junction of the input channel n.

Replacing the actual value of the reflection coefficient $r = -1/2$ in (2.48), we get

$$\left\{1 - \frac{1}{2}\cos\left[\beta(W-2d)\right]e^{-j\beta W}\right\} y_n - \frac{1}{4}e^{-j\beta W}y_{n-1} - \frac{1}{4}e^{-j\beta W}y_{n+1}$$
$$= je^{-j\beta W}\left\{x_n \sin[\beta(W-d)] + x_{n+1}\sin(\beta d)\right\}. \tag{2.50}$$

$$\left\{1 - \frac{1}{2}\cos\left[\beta(W-2d)\right]e^{-j\beta W}\right\} y_n - \frac{1}{4}e^{-j\beta W}\left(y_{n+1} + y_{n-1}\right)$$
$$= je^{-j\beta W}\left\{x_n \sin\left[\beta(W-d)\right] + x_{n+1}\sin(\beta d)\right\}. \tag{2.51}$$

The sinusoidal functions in the right-hand side of (2.51) are due to standing waves formed between the input channels. Such standing waves do not affect the operation of the structure, as under the condition $\beta(W-2d) = (2m+1)\pi$ the input term in (2.51) is still proportional to $x_{n+1} - x_n$.

2.5 Response Under Plane-wave Incidence

To gain further insight into the operation of the network, we study its response under plane-wave illumination with incidence angle θ and transverse wavenumber $k_{\rm t} = k\sin\theta$. Then, the signals at the input channels of the subtracting network have the form $x_n = x_0 e^{-jnk_{\rm t}W}$, where x_0 is a complex constant that is proportional to the incident field amplitude. Substituting this equation to (2.25), we find after some simple algebraic manipulations $|y_n|^2 \approx \sin^2\left(\frac{k_{\rm t}W}{2}\right)|x_0|^2$. We see that for $k_{\rm t} = 0$ the output signals are zero and increase as $k_{\rm t}$ increases, as expected from a derivative operation. The output signal takes its maximum value for $k_{\rm t} = \pi/W$, which, as discussed earlier, is the upper value of the transverse

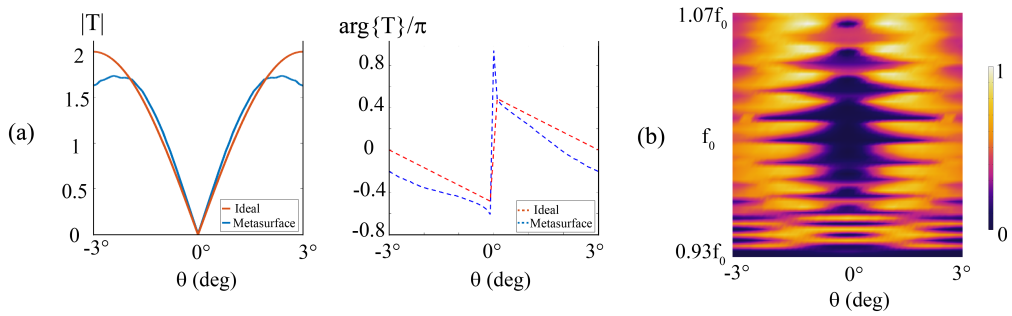

Figure 7: Response of the full structure (antenna array and ensuing waveguide). (a) Intensity and phase of the transmission coefficient compared to ideal difference response. (b) Transmission versus frequency and illumination angle.

wavenumber dictated by the Nyquist-Shannon sampling theorem. This fact shows that sampling according to the Nyquist-Shannon bound leads to the most efficient use of the structure. If sampling was faster, i.e., $W < \pi/k_{x,\max}$, the output from the subtracting network at the maximum wavenumber of the input image would be less than its maximum possible value, reducing the output signal intensity. Since we are dealing with passive structures, boosting the output signal in this case would require using a larger number of input signals beyond the nearest neighbor ones, increasing the order and therefore the complexity of the filter. Following the analysis used for the derivation of (2.51), we find that the full expression for the transmission coefficient valid at any frequency is given by

$$\begin{aligned} T(k_{\mathrm{t}},\beta) &= \frac{|y_0|^2}{|x_0|^2} \\ &= \frac{\left| e^{j\frac{\beta W}{2}} \cos\left[\frac{k_{\mathrm{t}}W-\beta(W-2d)}{2}\right] - e^{-j\frac{\beta W}{2}} \cos\left[\frac{k_{\mathrm{t}}W+\beta(W-2d)}{2}\right] \right|^2}{|\Delta(k_{\mathrm{t}},\beta)|^2}, \end{aligned} \tag{2.52}$$

where

$$\Delta(k_{\mathrm{t}},\beta) = 1 - \frac{1}{2}\left\{\cos(k_{\mathrm{t}}W) + \cos\left[\beta(W-2d)\right]\right\} e^{-j\beta W}. \tag{2.53}$$

Fig. 5b presents transmission versus frequency and incident angle obtained through (2.52) and full-wave simulations through Comsol Multiphysics for a structure designed to work for a maximum incident angle $\theta_{\max} = 3^\circ$. The theoretical and numerical results are in excellent agreement with each other. The response is symmetric with respect to $\theta = 0^\circ$, with transmission being close to zero at $\theta = 0^\circ$ and increasing as θ increases, as it should be for a difference operation. The resonant features are due to the standing-wave resonances between the input channels (the sinusoidal terms in the right-hand side in (2.51)). At the center frequency f_0, i.e., the frequency for which $\beta(W - 2d) = (2m + 1)\pi$ is satisfied, the angle of maximum transmission is $\theta = \pm 3^\circ$, per design, while as we move further from f_0, this angle slightly decreases. This response is maintained over a bandwidth of about 5% about f_0 (roughly speaking, the bandwidth of the center dark region in Fig. 5b), which is among the highest among all structures reported so far for edge detection. To gain a better understanding about the factors determining the bandwidth, we calculate the Taylor expansion of (2.51) with respect to β about it value β_0 at f_0. Keeping only the lowest-order terms, the result reads

$$T(k_{\rm t}, \beta) \approx T(k_{\rm t}, \beta_0) + \frac{\cos^2\left(\frac{k_{\rm t}W}{2}\right)\sin^2\left(\frac{\beta_0 W}{2}\right)}{|\Delta(k_{\rm t}, \beta_0)|^2}[\Delta\beta(W - 2d)]^2, \tag{2.54}$$

where $\Delta\beta = \beta - \beta_0$. For small $k_{\rm t}$, as here, $\cos^2(k_{\rm t}W/2) \approx 1$ and the second term in (2.54) represents a constant shift of the transmission level depending on β (frequency). Considering that $\beta = \sqrt{k^2\varepsilon_{\rm r} - (\pi/w_{\rm g})^2}$, where $w_{\rm g}$ is the width of the waveguide, we find $\Delta\beta \approx (k_0\varepsilon_r/\beta_0)(2\pi\Delta f/c)$, where $\Delta f = f - f_0$ and c is the speed of light. Assuming operation far from the waveguide cutoff frequency, it follows that the perturbation from

the ideal response is proportional to $\Delta f^2\sqrt{\varepsilon_r}(W-2d)^2$. Therefore the bandwidth increases, if we reduce ε_r or $W-2d$, with the latter condition achieved by selecting d as close as possible to $W/2$.

Next, we discuss the response of the complete structure, consisting of both the lens array and the subtracting waveguide. Fig. 7a shows the magnitude and phase of the transfer function versus the incidence angle at the center frequency f_0. The response was obtained through full-wave simulation with Comsol Multiphysics. In the same figure, we also plot the response expected for an ideal difference operation. The agreement between the ideal and numerical results is excellent. The intensity of transfer function is symmetric with respect to $\theta = 0^\circ$, as expected from (2.52) and in agreement with the ideal response. On the other hand, the phase is odd symmetric with respect to $\theta = 0^\circ$ as required for a first-derivative operation. Note that peak transmission is greater than 1, because the system funnels the incident power over one period to the much smaller area of the output channels. Fig. 7b shows the output power from the metasurface versus frequency and incident angle. The response is almost the same as for the subtracting waveguide and exhibits a bandwidth of about 5%.

To better see the effect of the metasurface on an incident image, Fig. 8 presents the output from the structure when the input is a 1-D image that includes constant, ramp, parabolic and sinusoidal functions. The results have been obtained for a broad range of frequencies and for three different image lengths. The image is selected so that for the smaller length the image's maximum spatial frequency is equal to the system's $k_{\mathrm{t,max}}$. Obviously, increasing the image length leads to a narrower spatial spectrum. The output images were obtained by multiplying the spatial Fourier transform of the input signal with

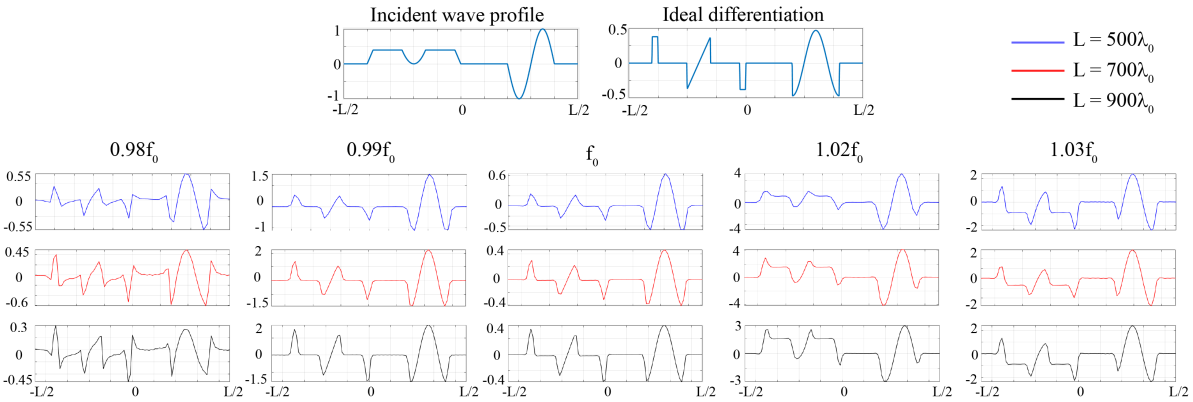

Figure 8: Response of the structure under illumination with a generic optical field. Three cases for the length of the input image are analyzed, 500λ, 700λ and 900λ, with the smallest length yielding an angular spectrum equal to the one of the structure. The results are derived for 5 different frequencies spanning the entire bandwidth of the structure. In all cases, the response is very close to the ideal difference response.

the system's transfer function and converting the result to spatial domain through an inverse Fourier transform. The proposed system is capable of performing high-quality edge detection for all lengths and frequencies, with the results being the best at the center frequency f_0, as expected. Note the proper edge detection performance with this range of frequency bandwidth and over a momentum spectrum with this level of proximity to null-momentum value, as is the case of projected images on typical sensor arrays, is pretty rare in the literature. As will be explained in the following, this fact makes the proposed system particularly suitable for integration with sensor arrays.

2.6 Photo-detection Integration and Numerical Aperture

The proposed approach can be seamlessly integrated with sensor arrays, if the periodicity of the system is selected to be equal to the pixel size of the array and the output apertures are aligned with the array sensors. In that sense, the proposed system shares similarities with the broadly-used Bayer filters, where each sensor is supplied with an extra absorptive layer or more sophisticated nanostructures, e.g., Fabry-Perot resonators, to

achieve color separation. Here we bring this approach one step further, by showing how it can be used for OSP. It is important to mention that our approach is more suitable for such integration than other OSP approaches, like those based on nonlocal metasurfaces.

Nonlocal metasurfaces are typically designed with a relatively large numerical aperture (NA), in the order of 0.3, corresponding to a maximum transverse wavenumber $k_{\mathrm{t,max}} = 0.3k$. On the other hand, a typical camera with a pixel size $\Delta = 5$ μm operating at the middle of the visible spectrum, 0.5 μm, can resolve images with a maximum wavenumber $k_{\mathrm{t,max}} = 1/(2\Delta) = 0.008k$, more than two orders of magnitude smaller than the maximum wavenumber of the metasurface, showing that only a very small fraction of the spatial spectrum of the metasurface around $k_{\mathrm{t}} = 0$ is actually used, which leads to small efficiency, since transmission around $k_{\mathrm{t}} = 0$ is very small. In principle, this problem can be overcome by designing the metasurface to have a small NA or alternatively speaking a spatial spectrum matching the one of the sensor array. This would require very

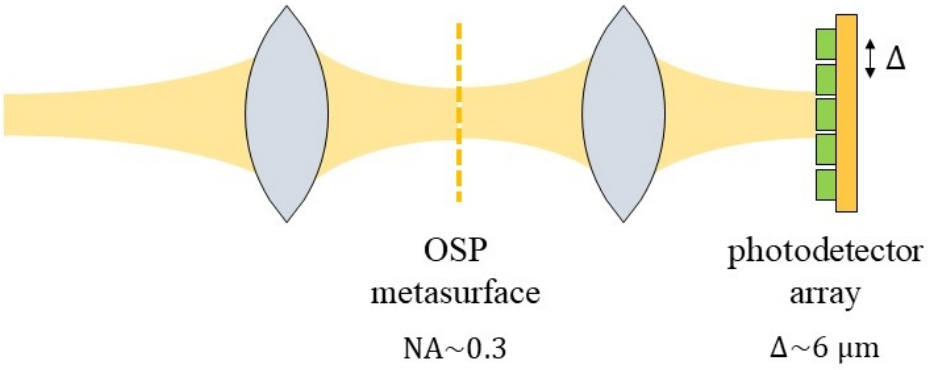

Figure 9: Sensor array integration with OSP approaches. Nonlocal metasurfaces are designed with a large numerical aperture (NA=0.3); much larger than the desired NA for an array with periodicity of 0.5 μm.

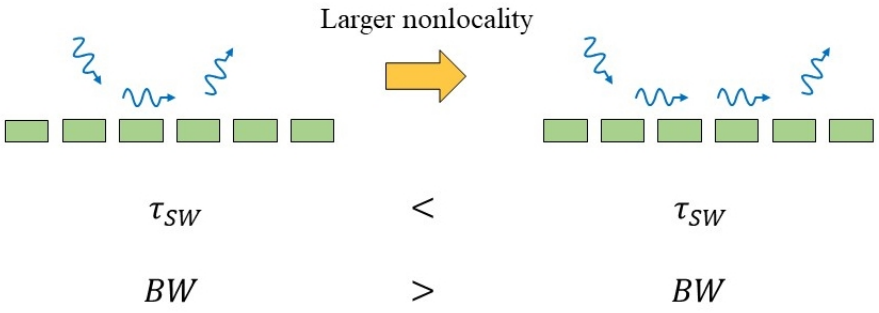

Figure 10: Trade-off between radiation decay rate τ_{sw} and temporal frequency bandwidth BW. Strong nonlocality needs large radiation decay and therefore narrow bandwidth. Looking at two extreme cases of τ_{sw} may provide a better insight into this trade-off. An impulse τ_{sw} as a function of time excites infinite number of frequencies (very large BW) and a constant τ_{sw} over time results a single frequency radiation (very small BW).

strong nonlocality, since transmission would have to change from 0 to 1 over a very small k_{t} range. For structures based on leaky-wave resonances, such strong nonlocality would necessarily translate to a smaller bandwidth, since the leaky wave would have to propagate over a longer distance along the metasurface before being converted to radiation, which is only possible by reducing the radiation decay rate and consequently the bandwidth. Our structure is free from this trade-off, because waves propagate as guided modes along the core waveguide of the structure.

CHAPTER 3 OPTICAL IMAGE COMPRESSION

Optical computing has emerged as a promising candidate to replace electronics in image processing. The work in this area has so far focused on simple operations, like edge detection, which can be realized with the intrinsic nonlocal response of metasurfaces. However, implementation of more complex operations is still an open problem. Here, combining concepts from filter theory, signal processing and optical network design, we present a general framework to realize advanced image processing with waves. We focus on the case of image compression and present a structure that realizes the second-scale Haar discrete wavelet transform in the optical domain over a volume that fits within the space of a camera. We demonstrate the efficacy of the structure by studying the statistics of an image before and after it is transmitted through the structure. The presented approach opens up a route to the development of a new class of wave-operated smart cameras with high speed and low power power consumption.

Optical computing (OC), i.e., the use of optical signals to perform mathematical operations, emerged several decades ago, when the capabilities of electronic computers were still limited [36, 37, 38, 2]. The systems that were proposed in these early works were typically based on Fourier optics and although they supported a wide range of operations, they were bulky. For this reason, the interest in them gradually diminished, as transistor technology advanced towards smaller and faster devices. However, the recent progress in optical nanotechnology combined with the fundamental limitations of digital computers resulting from Moore's law have brought this idea back to the spotlight [1, 39, 40, 41, 42, 43, 44, 45, 46, 47, 15, 48, 49, 50, 51, 52, 53, 54, 55, 56, 57, 58]. Al-

though the development of general-purpose optical computers might be out of reach now, due to the weak nature of optical nonlinearities that make the design of optical logical gates difficult, optical waves are ideal for the implementation of linear operations, i.e., matrix algebra, which are usually the most demanding operations of a computing system [59]. Building upon this fact, several works have proposed optical implementations of the matrix operations involved in deep learning networks [41, 44, 51, 52, 53] or image processing [1, 40, 42, 43, 45, 15, 60, 49, 54], with the latter mostly focusing on relatively simple operations, like edge detection, which can be realized with the intrinsic nonlocal responses of photonic metasurfaces. However, such responses follow specific patterns and cannot be used for the implementation of more complex operations. One solution to this problem is offered by the so-called discrete-space optical computing (DSOC) that was proposed in chapter 2. This method approaches OC as a digital filter in space and consists of discretizing a wave in space through an array of antennas and then implementing a desired linear operation on the discretized wave through a photonic structure with a discrete number of input and output ports. A second approach that can also implement general linear matrices was proposed in [44, 55] and is based on stacks of diffractive metasurfaces. Both of these approaches have the capability of realizing complex image operations for waves in free-space, which cannot be realized with other techniques.

An image processing operation of high complexity but also high practical significance is image compression[61]. Any communication system is characterized by an upper limit on its capacity, commonly known as Shannon's limit, which predicts a maximum rate for transmission of digital information depending on the signal to noise ratio. Approaching this limit typically requires some kind of encoding to remove redundancies in the input

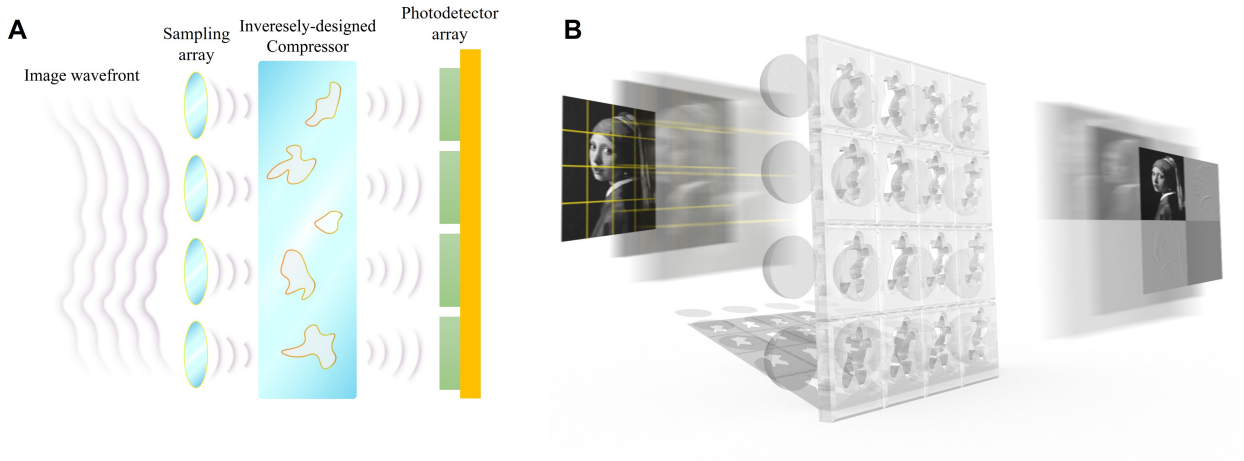

Figure 11: Conceptual illustration of an optical implementation of the DWT transform. (a) An incident wave is discretized in space through an array of lenses. The discrete outputs of the array are guided to a network with a discrete number of input and output ports that implements the Haar matrix. The output wave of the network are guided to a photodetector array. The periodicity of the lens array is the same as the one of the photodetector array. (b) Three-dimensional artistic rendering of the concept.

signal. For images, encoding is commonly referred as image compression and it exists in various forms, with the JPEG standard being the most popular one. An image compression system generally consists of two parts, one that performs a linear transformation, like the discrete wavelet transform (DWT), followed by a series of nonlinear operations that quantize and encode the output of the linear part. To date image compression is exclusively implemented in the digital domain. However, as a linear operation, the first block of an image compression system is suitable for an all-optical implementation, which can lead to a new class of smart imaging systems with high speed and low power consumption.

Here, we address this problem and show how the DWT, which is the most basic type of a linear transform in image compression, can be implemented in the optical domain through the DSOC approach in chapter 2. Our vision is outlined in Fig. **??** and consists of adding an optical structure designed to perform the DWT in front of the photodetector array of an

imaging system. Since the ultimate resolution of the system, i.e., the maximum transverse wavenumber of an input image that can be discriminated by the system, is determined by the photodetector array, in an optimal design the DWT structure should also have the same resolution. A mismatch between the resolutions of the OC structure and the photodetector array would require the addition of magnifying lenses between them, thus increasing the system's form factor. This requirement can be directly fulfilled with the DSOC approach, in which an incident wave is first sampled in space with a periodicity equal to the periodicity of the photodetector array and then the desired OC operation is performed on the resulting spatially discretized signal. An illustration of this approach is presented in Fig. 11(a). An optical wave is incident on an array of optical antennas, which can be a simple lens array, as in Fig. 11(a), or of a more sophisticated form, as will be presented later in this chapter. The purpose of the array is to periodically sample an incident wave in space. The output signals of the array are then directed to a second network with a discrete number of input and output ports that implements the desired linear operation, which in our case is the DWT. As will be shown in the following, this approach allows implementing high-quality lossless image compression exclusively in the optical domain over a compact volume, which in addition to its own merit as the first all-optical realization of image compression lays the ground work towards the realization of also other operations for imaging systems. In signal processing the DWT is usually defined through a series of successive low- and high-pass filtering operations, followed by down-sampling operations [61, 62]. If this process is applied P times, the DWT is said to have a scale P. Although this definition is ideal for a software implementation of the DWT, for an optical implementation the transform has to be expressed in a matrix form. For example, for one-dimensional signals the transform

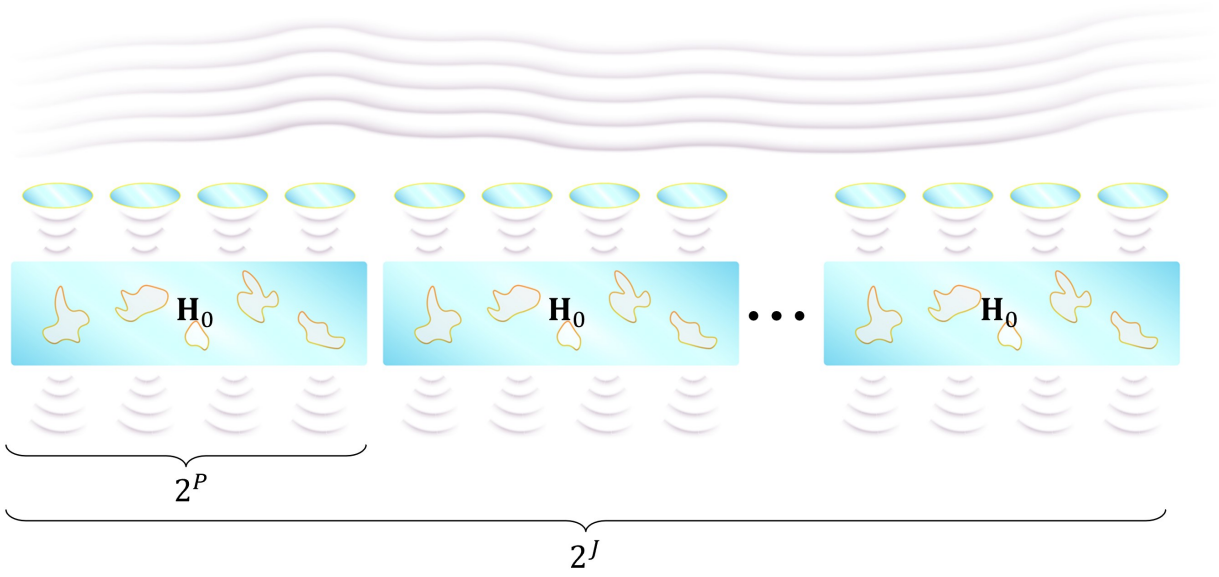

Figure 12: Optical implementation of the one-dimensional Haar DWT transform of scale P for a system with 2^J pixels. The structure is a combination of 2^{J-P} identical networks each of which has 2^P input and 2^P output ports and a transformation matrix $\mathbf{H}_0$ equal to the Haar matrix.

has to be expressed in the form $\mathbf{Y} = \mathbf{HX}$, where $\mathbf{X}$ is an input signal of length N, $\mathbf{Y}$ is the output signal of the same length as $\mathbf{X}$, and $\mathbf{H}$ is a $N \times N$ matrix representing the transform. Taking N to be a power of 2, i.e., $N = 2^J$, as is usually the case, the matrix of the transform can be written as

$$\mathbf{H} = \begin{bmatrix} \mathbf{H}_0 & \mathbf{H}_1 & \mathbf{H}_2 & \dots \\ \mathbf{H}_{-1} & \mathbf{H}_0 & \mathbf{H}_1 & \dots \\ \mathbf{H}_{-2} & \mathbf{H}_{-1} & \mathbf{H}_0 & \dots \\ \vdots & \vdots & \vdots & \ddots \end{bmatrix}, \tag{3.1}$$

where $\mathbf{H}_i$ are square matrices of size $2^P \times 2^P$. For a general DWT, an optical implementation of $\mathbf{H}$ would require a network with 2^N input and 2^N output ports, which might be difficult to realize for systems with a large number of pixels. However, there is a specific case of a DWT, yet of high practical significance, where the form of $\mathbf{H}$ simplifies to a significant

degree. This is the so-called Haar transform, for which all the off-diagonal elements of $\mathbf{H}$ are zero, i.e., $\mathbf{H}_i = \mathbf{0}$ for $i \neq 0$. In this case $\mathbf{H}$ reduces to a block diagonal matrix with $\mathbf{H}_0$ as the diagonal elements of the matrix. Then, an optical implementation of $\mathbf{H}$ would consist of 2^{N-P} identical networks, each of which realizes $\mathbf{H}_0$ and has 2^P input and 2^P output ports, as shown in Fig. 12. Therefore, the complexity of a Haar transform is 2^{N-P} times smaller than a general DWT, making it a particularly attractive transform for an optical implementation.

Following these remarks, here, we demonstrate an optical implementation of the second-level ($P = 2$) Haar transform with a matrix

$$\mathbf{H}_0 = \frac{1}{2}\begin{bmatrix} 1 & 1 & 1 & 1 \\ 1 & 1 & -1 & -1 \\ \sqrt{2} & -\sqrt{2} & 0 & 0 \\ 0 & 0 & \sqrt{2} & -\sqrt{2} \end{bmatrix}. \tag{3.2}$$

This matrix is unitary, which means that it can be realized with a passive optical network. To design such a network, we use two-dimensional topology optimization [63], assuming dielectric waveguides as input and output ports and a material with a relative electric permittivity of 2.26 (polypropylene). We start with the design of the lens array by invoking as a requirement that each lens converts an incident Gaussian beam to the fundamental mode of the input waveguides of the computing part of the system. Although in principle it is possible to use conventional lenses for the lens array, here we prefer custom-designed ones because they lead to a smaller form factor. The lenses are shown in Fig. 14a and have dimensions $2.82\lambda \times 3.34\lambda$, significantly smaller than the dimensions of a conventional lens

used in chapter 2. By applying the Lorentz reciprocity theorem, the output of these lenses is approximately found as

$$x_n \approx \frac{\int E_{\text{inc}}(x) W(x - na) dx}{\int [W(x)]^2 dx}, \tag{3.3}$$

where $E_{\text{inc}}(x)$ is the incident field, $W(x) = \exp(-x^2/w_0^2)$ is the profile of the incident Gaussian beam, w_0 is the beam waist which is 0.95λ, n is an index for the lenses, and a is the periodicity of the array. For the computing part of the system, we assume four input and four output ports and invoke as a requirement that the input-output matrix is equal to the Haar matrix in Eq. (B.24). The structure obtained through this procedure is shown in Fig. 14(a) and exhibits a transmission matrix

$$\tilde{\mathbf{H}}_0 = \frac{1}{2} \begin{bmatrix} 0.956e^{i0^\circ} & 0.934e^{-i2^\circ} & 0.940e^{-i3^\circ} & 0.920e^{-i2^\circ} \\ 0.936e^{-i2^\circ} & 0.959e^{-i2^\circ} & 0.923e^{i178^\circ} & 0.929e^{i178^\circ} \\ 0.908\sqrt{2}e^{-i2^\circ} & 0.916\sqrt{2}e^{i179^\circ} & 0.072e^{i48^\circ} & 0.088e^{-i90^\circ} \\ 0.082e^{i111^\circ} & 0.093e^{-i71^\circ} & 0.918\sqrt{2}e^{-i1^\circ} & 0.929\sqrt{2}e^{i178^\circ} \end{bmatrix}, \tag{3.4}$$

which is very close to the Haar DWT matrix. Fig. 13 shows filed distribution of simulated

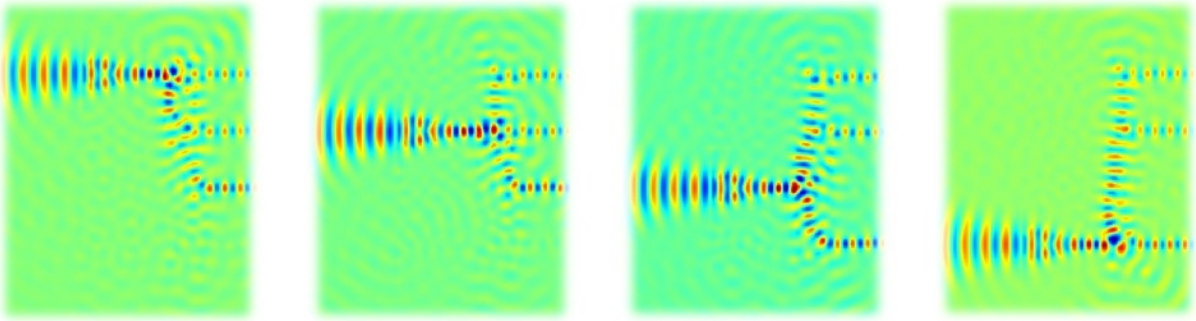

Figure 13: Field distribution of combined lens array and Haar transformer metamaterials. Lens are individually excited by Gaussian beams of unitary power.

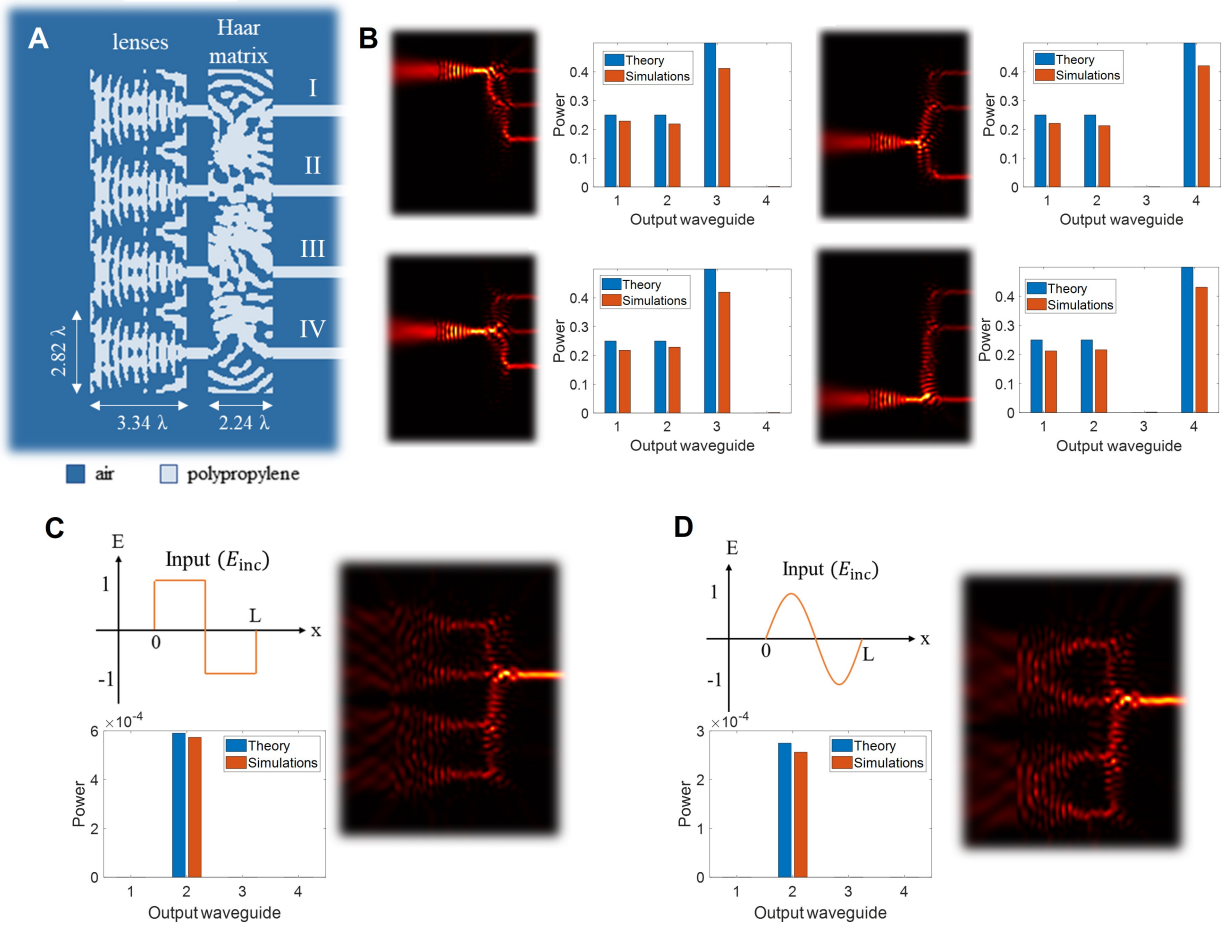

Figure 14: Constituent block of the optical implementation of the two-level Haar transform. (a) Structure of the block. (b) Simulation results for excitation with Gaussian beams for a different lens at a time. The bar diagrams compare the output power from simulations and from the ideal Haar matrix (Eq. (B.24)). (c) Simulation results for an incident wave modeling a 4-pixel image with a pixel vector $[1\,1\,-1\,-1]$. The bar diagram compares the power from simulations and the one calculated from the Haar matrix in Eq. (3.4) for an input vector calculated as the weighted average of the incident wave according to Eq. (3.3). (d) The same as (c), but for a sinusoidal incident wave representing a smoothened version of the same input image.

metamaterial. Intensity routing to output waveguides and phase difference desired to implement Haar transformations can be understood here.

To assess the efficacy of the system, we perform full-wave simulations for excitation from one lens at a time with incident waves the Gaussian beams used in the design of the lenses. The results are presented in Fig. 14(b). The output signals for excitation from

the i-th lens are expected to match the i-th column of the Haar matrix, which can be seen to be the case. As a more realistic case, we consider an incident wave spanning the entire structure with a square-pulse profile representing a 4-pixel image with a pixel vector $[1\,1\,-1\,-1]$ as in Fig. 14(c). The output power is compared with the output power obtained from the ideal Haar matrix in Eq. (B.24) for an input vector obtained through weighted averaging of the incident wave according to Eq. (3.3). The agreement between the two results is excellent. Finally, Fig. 14(d) presents a similar analysis as Fig. 14(c), but with a smoothed out profile for the incident wave, as expected in reality. The results match the ideal result even in this case, with the exception of lower output power due to the smaller overlap of the incident wave with the weighting function that results in a smaller efficiency for the lenses.

To better see the compression capabilities of the system, we analyze its effect on a two-dimensional image as in Fig. 15(a). For this analysis it is assumed that the structure is a two-dimensional array of blocks, like the ones in Fig. 14a, with $N_x/4$ and N_y blocks in the x and y directions, with N_x and N_y the numbers of pixels of the input image in these directions. The analysis assumes that the incident wave is a superposition of non-overlapping square pulses with widths equal to the widths of the lenses and amplitudes proportional to the grey-scale levels of the input image's pixels. Although in reality the incident wave is expected to have a smooth profile, as discussed earlier this has no effect on the output of the structure, other than a constant reduction of all outputs signals. The output of the structure is obtained by applying the simulated matrix in Eq. (3.4) to the weighted-average of the incident wave, considering that as demonstrated earlier such a procedure leads to results fairly close to full-wave simulations. The output image obtained

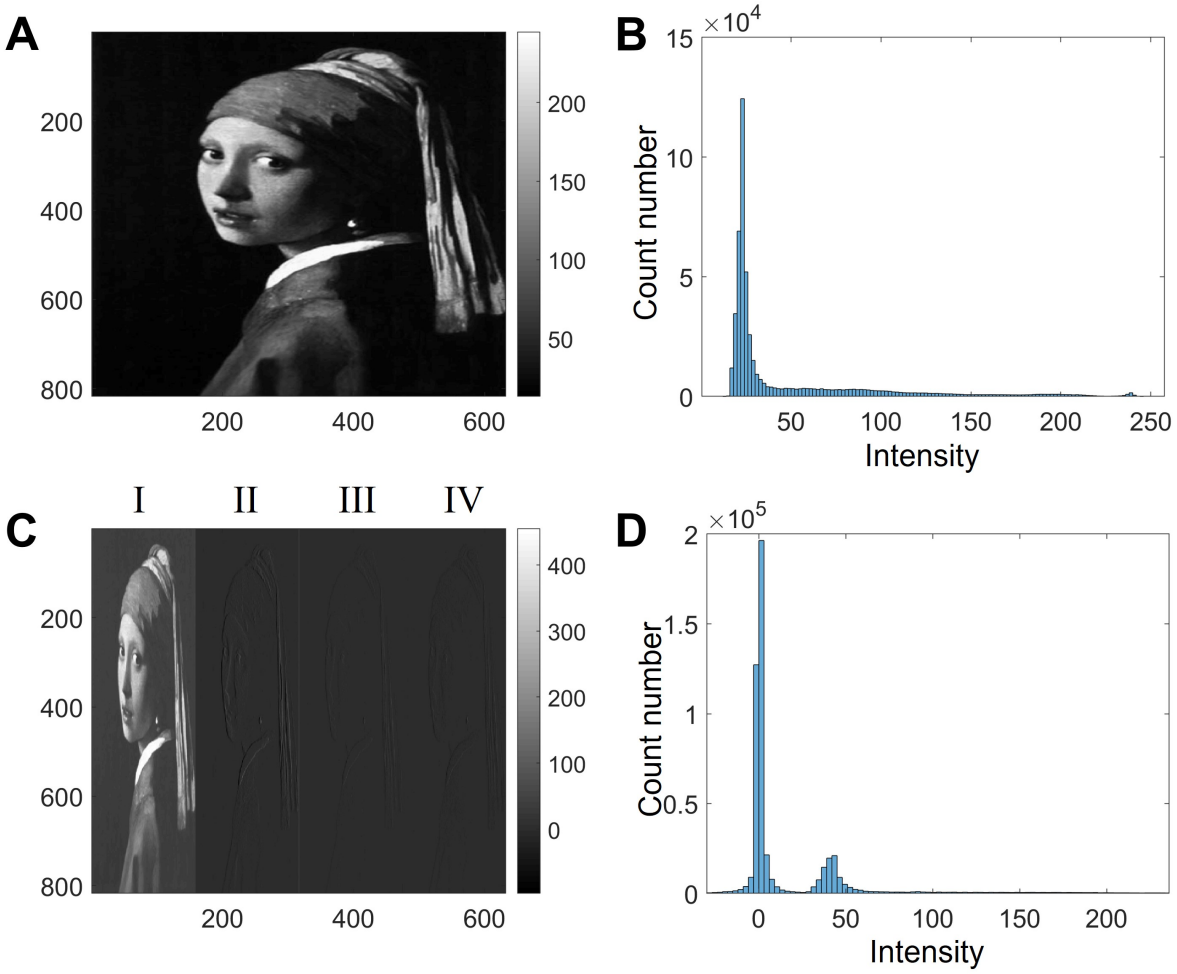

Figure 15: Operation of the optical implementation of the Haar transform on an image. (a) Input image. (b) Histogram of the input image. (c) Output image. (d) Histogram of the output image. The Haar transform is applied to the rows of the input image.

through this procedure is shown in Fig. 15b, where for visualization purposes the output signals from different blocks have been grouped according to the output port of each block, i.e., ports I, II, III, and IV as defined in Fig. 14a. Note that the output image, i.e., the four sub-images combined, is of the same size as the input one. A visual inspection of the output image immediately reveals that it contains a larger number of low-intensity levels, which require a smaller number of information bits for their encoding, than the input image. This fact is better understood by inspecting the histograms of the input and

output images, representing the number of times each intensity level appears in the image. An image with a narrower histogram can be encoded with a smaller number of bits than one with a broader histogram. Therefore, the effect of image compression can be assessed by looking at the width of the histogram before and after the transformation. This is the case in Fig. 15, where the output histogram is narrower than the input one. For a more quantitative assessment of the system's compression capability we use the information entropy, defined as

$$H = -\sum_{i=1}^{n} p_i \log_2(p_i), \tag{3.5}$$

where p_i is the probability of the i-th intensity level to be found in an image. For the original and compressed images in Fig. 15 the information entropy is 4.74 bits/pixel and 3.58 bits/pixel, respectively, representing a 24% reduction of spatial redundancy after the Haar transformation. Larger degrees of compression can be achieved by increasing the scale of the transform or through two-dimensional transforms.

In addition to their significance as the first optical implementation of image compression, the results presented here constitute a significant leap forward in the area of OSP, since they demonstrate the feasibility of optical implementation of advanced imaging operations beyond those that are possible through the innate nonlocal responses of optical structures. Such a task is made possible by combining concepts from filter theory, signal processing and photonic network design, together with the flexibility offered by topology optimization for the design of arbitrary photonic networks. The framework presented here is general, can in principle be applied to any imaging operation that can be described through a linear matrix operation, and is suitable for realization with additive manufac-

turing. Furthermore, it can be directly integrated in the architecture of imaging systems without affecting their size. We believe that the results presented here can inspire a new class of smart cameras with advanced computational capabilities, high speeds and low power consumption.

CHAPTER 4 RGB TO YUV ALL-OPTICAL COLOR ENCODING

RGB is a color encoding method where a colored image is made of red, green, and blue images. Each individual pixel color is expressed by proper weighting coefficients of these colors. Many electronic devices we use every day use RGB to record or display colored images. RGB while being significantly useful, does not offer direct control over brightness and is not the most reliable when it comes to telecommunication bandwidth. YUV color encoding model is another popular method to represent colored images. Unlike RGB, YUV provides brightness control by devoting one dimension to brightness and the other two dimensions to the color component of an image. For example, a black and white screen can properly work by only controlling the brightness dimension (Y) of this encoding. Fig. 16 shows the mapping between the U and V dimensions of this scheme and color, and an example of a YUV decomposition of a sample image. In digital image processing, the RGB to YUV transformation is defined as

$$\begin{bmatrix} Y \\ U \\ V \end{bmatrix} = \begin{bmatrix} 0.299 & 0.587 & 0.114 \\ -0.14713 & -0.28886 & 0.436 \\ 0.615 & -0.51499 & -0.10001 \end{bmatrix} \begin{bmatrix} R \\ G \\ B \end{bmatrix} \tag{4.1}$$

The YUV dimensions have upper and lower bounds as $0 \leq Y \leq 1$, $|U| \leq U_{max}$ and $|V| \leq V_{max}$, where $U_{max} = 0.436$ and $V_{max} = 0.615$.

Inspired by this digital transformation, we apply the discrete-space approach to color encoding. The idea is to implement the transfer function on a photonic platform. Due to the complexity of the transfer function, once again we reflect back to inverse topology optimization as our designer method. However, there is a complication with an optical

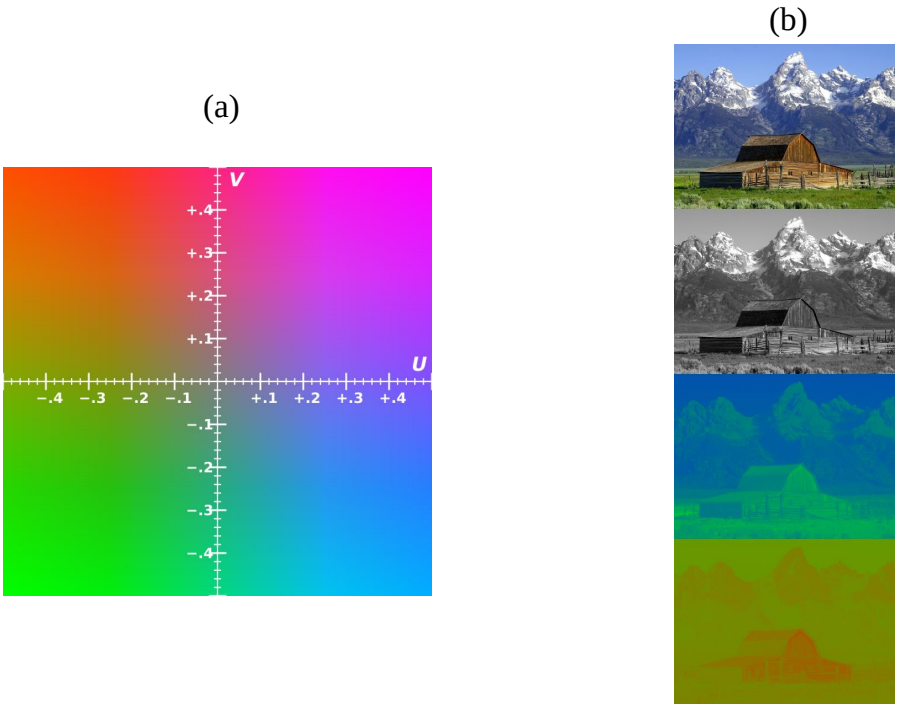

Figure 16: (a) Representation of chromatic dimensions of YUV color encoding model. V-U plane colorcode distribution changes with Y variation. Here, V-U is plotted at Y=0.5. (b) A sample image encoded in YUV model. Credit to Wikipedia

implementation of the YUV transformation, nameley the fact that it does not satisfy power conservation. Therefore, we make slight manipulation to the matrix to accomplish power conservation. First we scale the output Y, U, and V components of the transformation by coefficients γ_1, γ_2, and γ_3, respectively. Such a scaling does not alter the essense of the transformation, since it can be incorporated in the measurement protocol of the output signals. Furthermore, since a measurement is usually performed on power, we translate the U and V components of the transformation matrix (second and third row of the matrix)

by U_{max} and $V_{\max}$. Then, the modified transfer function is

$$\mathbf{H_{mod}} = \mathbf{S} = \begin{bmatrix} 0.299\gamma_1 & 0.587\gamma_1 & 0.114\gamma_1 \\ (-0.14713 + U_{max})\gamma_2 & (-0.28886 + U_{max})\gamma_2 & (0.436 + U_{max})\gamma_2 \\ 0.615 + V_{max})\gamma_3 & (-0.51499 + V_{max})\gamma_3 & (-0.10001 + V_{max})\gamma_3 \end{bmatrix}. \tag{4.2}$$

This matrix is defined for power at different wavelengths and as a result power conservation needs to be applied independently at each wavelength. Specifically, assuming three independent excitations at the wavelengths of the R, G and B components, described through the input vectors $\binom{R}{G}{B} = \binom{1}{0}{0}$, $\binom{R}{G}{B} = \binom{0}{1}{0}$ and $\binom{R}{G}{B} = \binom{0}{0}{1}$, we ask that $|Y|^2 + |U|^2 + |V|^2 = 1$ for each excitation. Then, the γ coefficients are determined as

$$\gamma = \begin{bmatrix} 1.45782 \\ 0.79571 \\ 0.27175 \end{bmatrix} \tag{4.3}$$

and the modified transfer function which is given by

$$\mathbf{S} = \begin{bmatrix} 0.660 & 0.925 & 0.408 \\ 0.479 & 0.342 & 0.833 \\ 0.578 & 0.165 & 0.374 \end{bmatrix}. \tag{4.4}$$

Again, it is important to stress that this matrix is defined with respect to the moduli of waves at different frequencies and therefore it does not need to satisfy the conventional unitarity condition of scattering matrices defined for complex amplitudes at the same frequency.

To realize the matrix in Eq. (4.4) we follow a two-step approach. First, the R, G, and B frequency components of an incident wave first are demultiplexed to signals at three different ports. The design of the demultiplexer was performed by assuming wavelengths 1948 nm, 1648 nm and 1500 nm for the R, G and B components and using topology optimization to route each wavelength component of an input wave to a different port. Note that our design procedure is salable regarding the frequency and the metamaterial can be redesigned at any other part of the electromagnetic spectrum. Fig 17 presents the obtained design and simulations for each of the targeted wavelengths. At each iteration of the inverse-design, the metamaterial is excited with three Gaussian beams of the targetted wavelengths. Excitation Gaussian beams all contain unitary power and a $3\lambda/\pi$ width. The optimization objective is set to achieve close to unitary output power for each wavelength at its assigned waveguide port and nezr-zero transmission at the other ports. The demultiplexer is capable of wavelength separation at all three of wavelengths of our interest with more that 84% transmission efficiency.

Once the demultiplexer is designed, we shift our focus to network implementing the RGB to YUV transformation. To gain a better understanding of objective output waveguide

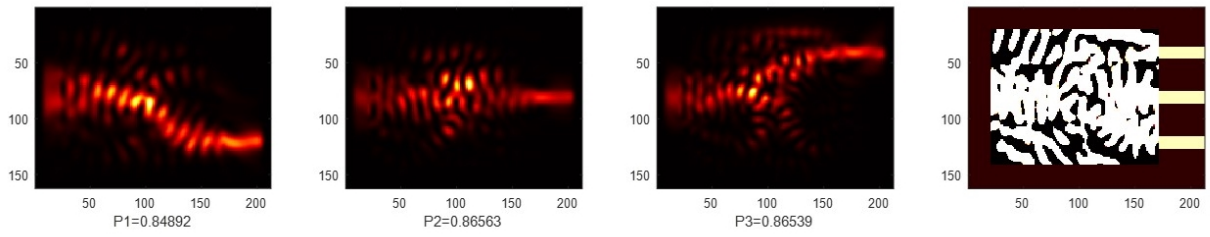

Figure 17: 1 to 3 Gaussian beam to waveguide mode wavelength demultiplexer. Input Gaussian beams share the same beam opening with respect to λ. That is the reason the actual beam opening in the simulations look to have different lengths. Color Separation efficient for $1948nm$, $1648nm$ and $1500nm$ are $\%85$, $\%87$ and $\%87$, respectively.

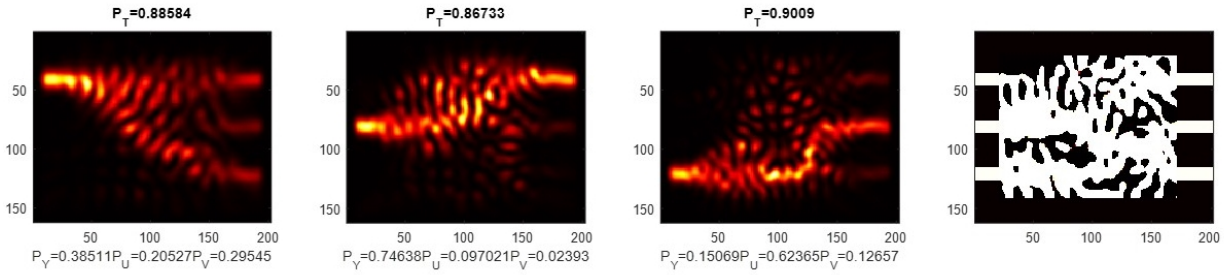

Figure 18: RGB to YUV transformer metamaterial. Wavveguide modes at $1948nm$, $1648nm$ and $1500nm$ with unitary powers excite the metamaterial while outputs are optimized to converge to columns of matrix P at each wavelength. The metamaterial shows overall efficiency of $\%89$, $\%87$ and $\%90$ at each wavelength respectively. The binary material takes $\epsilon_r = 1$ and $\epsilon_r = 2.26$.

powers for each wavelength excitation, the scattering matrix in Eq. 4.4 is converted to a power transmission matrix as

$$\mathbf{P} = \begin{bmatrix} 0.43589 & 0.85574 & 0.16619 \\ 0.22986 & 0.11708 & 0.69386 \\ 0.33425 & 0.02717 & 0.13995 \end{bmatrix}. \tag{4.5}$$

where each column adds up to one, in accordance with power conservation. Columns show how power is distributed among output wavegudes at each wavelength. $\mathbf{P}$ is introduced to the topology optimization as an objective goal and results are shown in Fig. 18. For this block, the inputs are the same waveguide modes as the outputs of frequency multiplexer metamaterial. This RGB to YUV metamaterial block reaches a power distribution matrix of

$$\mathbf{P_{meta}} = \begin{bmatrix} 0.38511 & 0.74464 & 0.15069 \\ 0.20527 & 0.09702 & 0.62365 \\ 0.29545 & 0.02393 & 0.12657 \end{bmatrix}. \tag{4.6}$$

To provide a better insight into the metamaterial operation, a comparison of ideal YUV

color encoding and encoding realized by the proposed metamaterial is shown in Fig. 19. Fig. 19a and b show the original image in its RGB decomposition. Fig. 19n and c are YUV decomposition for ideal case and transmission through the metamaterial. Note that all colorbars follow gray scale representation. Comparing results, there is a good agreement between ideal and metamaterial results indicating proper color encoding performance of the proposed metamaterial.

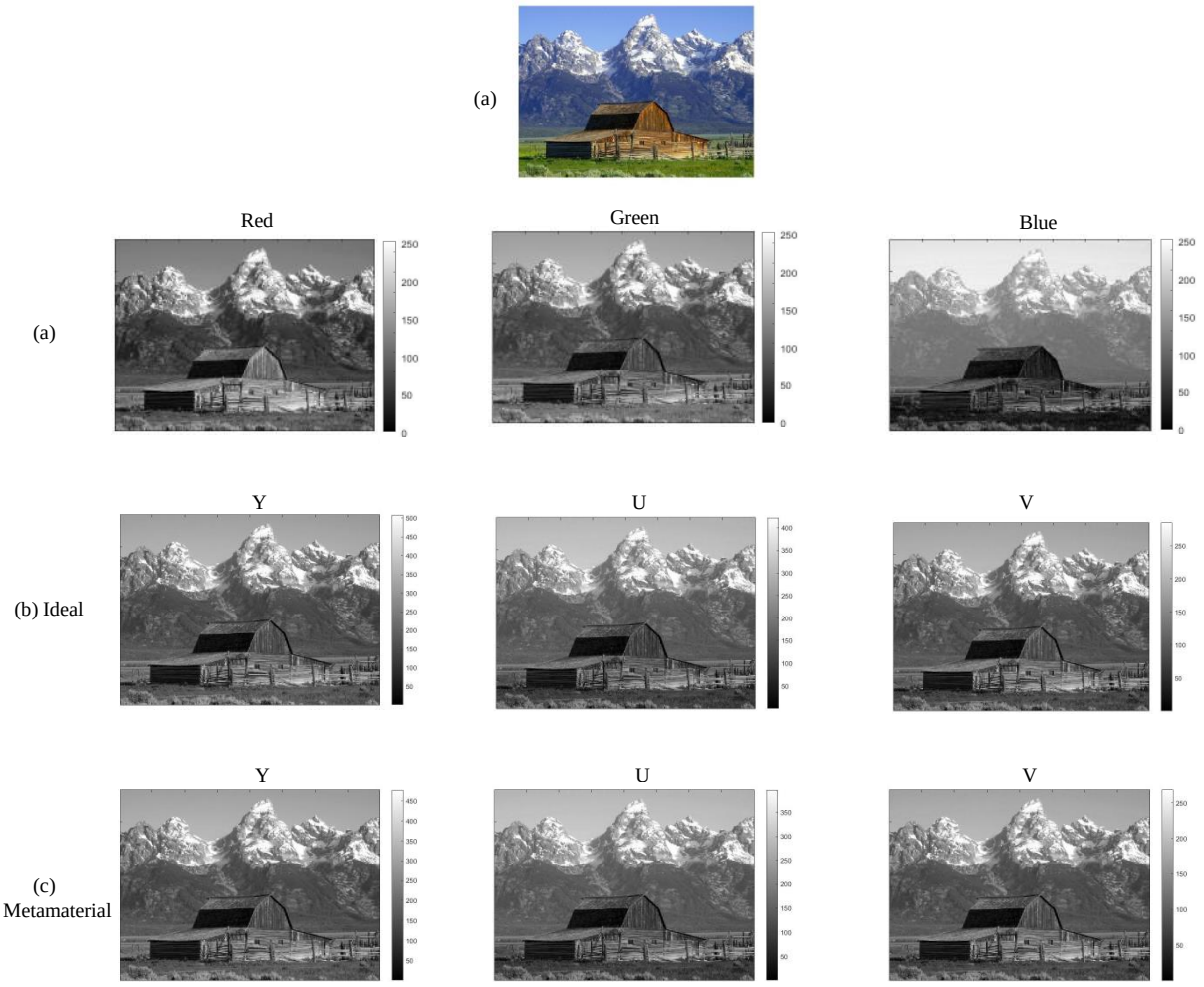

Figure 19: (a) Original image. (b) RGB representation. (c) Ideal YUV components. (d) Transformed YUV obtained from the inverse-designed metamaterial.

CHAPTER 5 HIGH IMPEDANCE MATCHING METAMATERIALS WITH TOPOLOGY OPTIMIZATION

Receive and transmission ends are essential units of any Radio Frequency (RF) wireless communication system. Due to the nature of propagating waves in air over long distances along with environmental conditions such as buildings, geographical obstacles and extreme weather conditions, RF receivers often are exposed with information signals with weak amplitude at the antenna front end. Therefore, use of a Low Noise Amplifier (LNA) right after the antenna is inevitable. Careful design of the receiving antenna along with proper matching network between the antenna and LNA play a significant role in maximizing the receiver efficiency. As we already deal with weak signals, any reflection at the LNA input is highly undesirable. This is important when we know low efficiency of every single block in a communication system may result in efficiency decrease of the entire system. Antenna design engineering with variety of efficient techniques is capable of offering devices with high receiving efficiency. Unfortunately, that is not the case for the matching network in between. LNAs often have matching circuits and transistors as

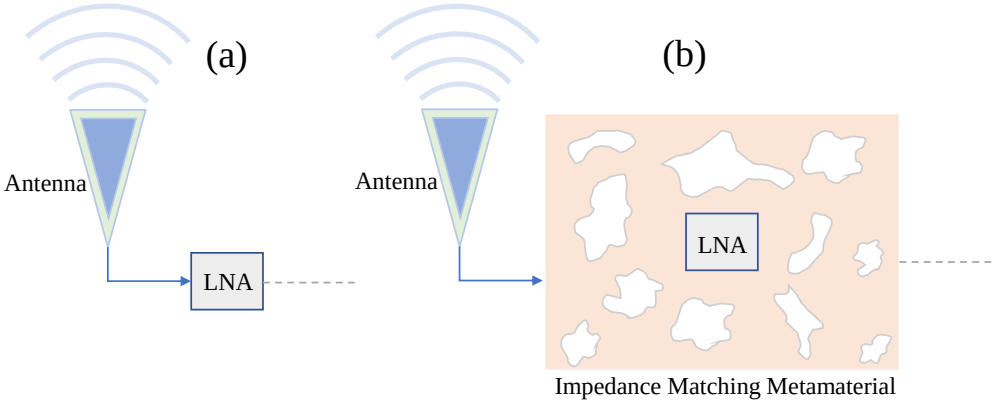

Figure 20: (a) Receiver front end of a conventional communication system. (b) Proposed idea to maximize high impedance matching with inverse-design metamaterials.

their first internal block. It is well-known that transistors in general have significantly high input impedance ($Z_{in} > 10^4\ \Omega$) for small signals, which causes significant mismatch to the antenna output which has a $50 - 100\ \Omega$ impedance. A schematic representation of conventional RF receivers is shown in Fig. 20a. With the great potential inverse topology optimization has brought to metamaterial design, we were curious whether it is possible to propose a metamaterial to maximize wave coupling between an antenna and a high impedance load. With that in mind, we propose the idea of warping the LNA in a matching inverse-designed metamaterial. Fig. 20b illustrates the proposed matching block. This specific design configuration is chosen since usually the LNA input has a coaxial cable shape, and therefore, the metamaterial surrounding the cable is expected to show higher efficiency to occupying area ratio.

Unlike previous inverse-design projects in this thesis, here the desired parameter is not the intensity and/or phase of some output waveguides. Here, the input power should be focused on a single lossy point with a fixed impedance, modeling for example the end of a metallic probe to which a circuit is connected. To keep the analysis simple, we assume a two-dimensional environment, that is one that is uniform along one axis, e.g., the y-axis. To understand the form of a metallic probe in such a case we invoke the equivalence between a two-dimensional environment with the physically-realizable environment of a parallel plate waveguide under operation with the fundamental mode only, which is know to have an electric field perpendicular to the plates of the waveguide. A metallic probe in such a case takes the form of a metallic wire connecting the plates of the waveguide with a small gap in the middle where the impedance is connected. By applying image theory we can convert this wire to one that is infinite along the z-axis, as in

Fig. 21. The current flowing through such a wire is given by $I = V/Z$, where Z is the load impedance and V the voltage across the gap where the load is connected, which is equal to $V = \int_{gap} \overline{E}_{gap} \cdot \overline{dl} \approx E\delta$, where $\overline{E}_{gap}$ is the electric field across the gap and δ the width of the gap. If the periodicity h of the periodically loaded wire, which is obviously equal to the height of the parallel-plate waveguide mode, is much smaller than the wavelength, the electric field is parallel to the wire (this statement is equivalent to claiming that the parallel-plate waveguide supports only the fundamental mode) and $V = E_{eff}h$, where E_{eff} is the average vertical electric field parallel to the wire. Then, we can express the current with respect to the electric field as

$$I = \frac{hE_{eff}}{Z}. \tag{5.1}$$

The power received by the wire can be obtained through the general formula for the power absorbed by a volumetric current density

$$P = \oint_V Re\{\bar{J}.\bar{E}^*\}dv \tag{5.2}$$

Applying this formula to the periodically loaded wire with the current obtained above, we find

$$P = \frac{h}{2}\frac{Re\{Z\}}{|Z|^2}|E_{eff}|^2. \tag{5.3}$$

A tricky point in the preceding analysis is the computation E_{eff} in a two-dimensional formulation of the problem. We know that E_{eff} is the average electric field parallel to the wire, but this definition requires knowledge of the field in three-dimensional space, which

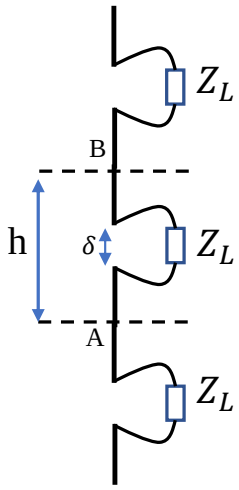

Figure 21: Circuit model of coaxial cable input impedance penetrating a parallel plate waveguide to harvest input power. The actual electric field has a non-zero value only along δ. Effective electric field used to make the connection between the physical and numerical model is and average electric field over the waveguide cross-section with length h.

we want to avoid, since that would make necessary a three-dimensional analysis. The answer to this problem is provided by Eq. (5.1). In a numerical analysis with the FDTD method, the two-dimensional space is discretized to elements with dimensions Δ_x and Δ_z in the x and z directions. In the case of a TE mode, the electric field has a z component and the magnetic field has components in both x and y directions. Fig. 22 shows how those components are arranged in a Yee grid arrangement. According to Ampere's law, integration of the magnetic field components along the boundary of a unit cell surrounding the wire results in

$$I = \oint_C \bar{H} \cdot d\bar{l} = \frac{hE_{eff}}{Z} \tag{5.4}$$

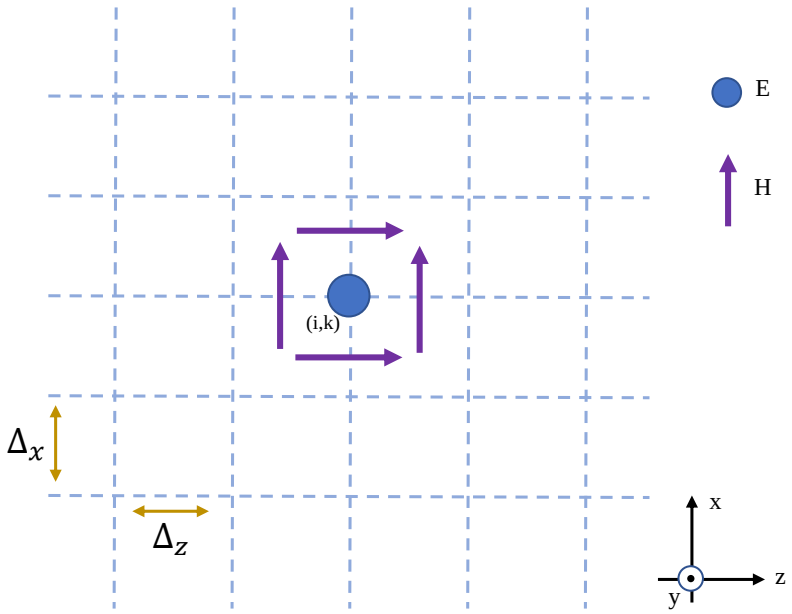

Figure 22: FDFD discretization grid and TE field components arrangement. Lossy ϵ_{eff} is a fixed boundary condition only at point (i, k) while permittivty at other ponts of the grid go through inverse topology optimization with no impedance constraint.

On the other hand, from the integral form of Maxwell equations we have

$$I = j\omega\epsilon_{effS}\bar{E} \cdot d\bar{S} = j\omega\epsilon_{eff}E_{eff}\Delta_x\Delta_z, \tag{5.5}$$

where ϵ_{eff} is an effective permittivity for the unit cell that contains the wire. Comparing the above equations we find that in a two-dimensional environment the wire can be modeled through an effective permittivity

$$\epsilon_{eff} = \frac{h}{j\omega Z\Delta x\Delta z}. \tag{5.6}$$

The effective permittivity model derived above is used in an inverse design algorithm to

design metamaterials that are able to convert an incident wave to a signal at the load with the highest possible efficiency. Specifically, an impedance loaded wire, modeled through Eq. (5.6), is surrounded by a square domain on which topology optimization is applied.

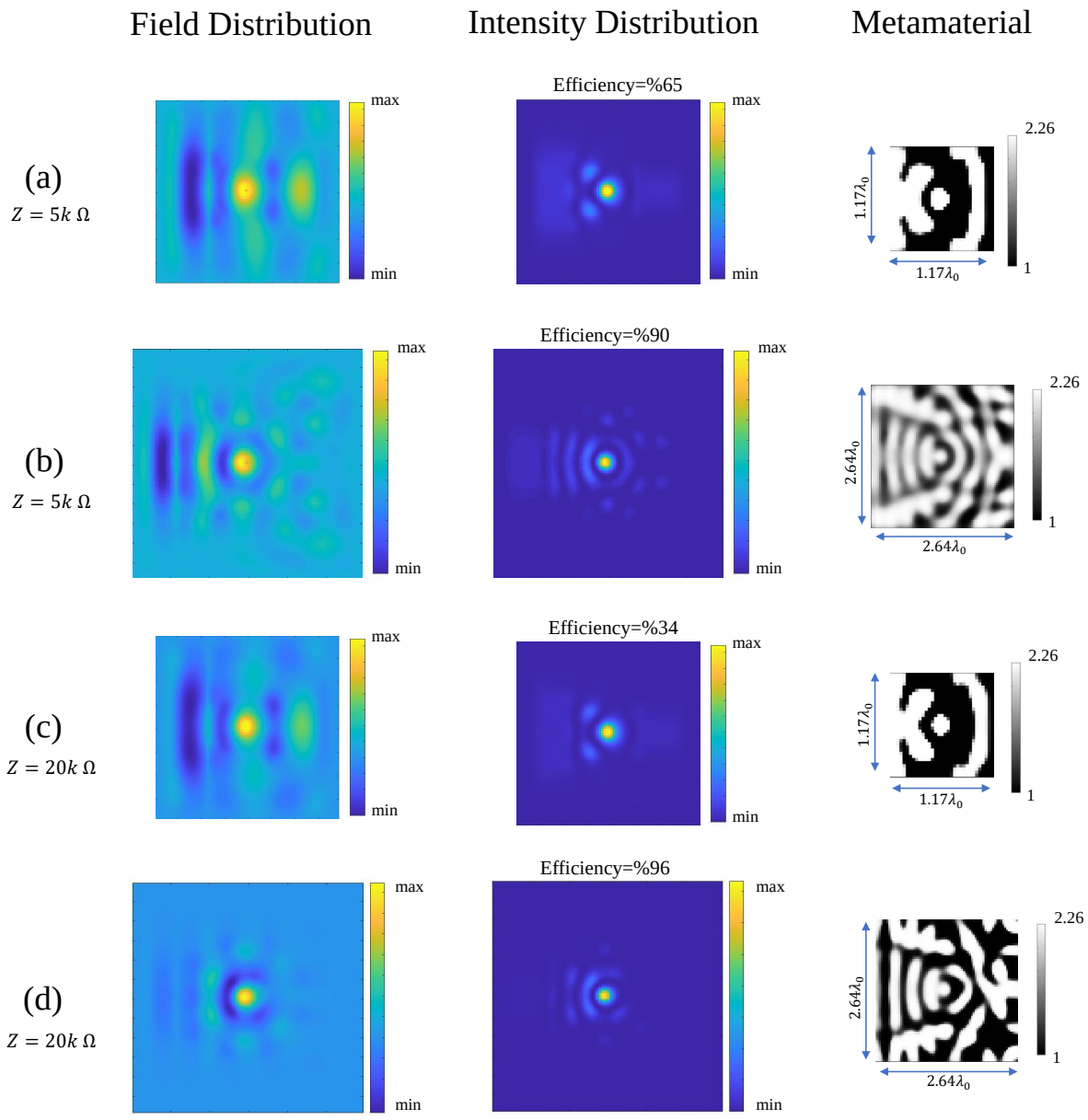

Figure 23: Field, intensity and topology comparison of impedance matching metamaterial for loads $Z = 5k\Omega$ and $Z = 20k\Omega$. Topology optimization is performed for two sizes of optimization domain ($2.64\lambda_0$ and $1.17\lambda_0$) to illustrate fundamental limits.

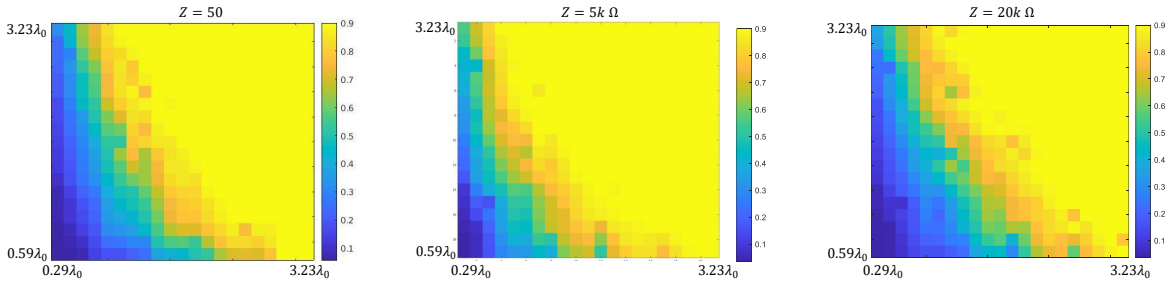

Figure 24: Gaussian input to load impedance coupling efficiency vs dimensions of rectangular optimization domain. The study minimized a proper cost function for 3000 iterations or stops each loop upon reaching $\%90$ efficiency.

For the excitation of the domain we use a Gaussian beam with a width of $3\lambda_0/\pi$ and unitary power. As a first example, we aim at designing a structure for matching the input beam to a load with $Z = 5$ kΩ and $Z = 20$ kΩ for square optimization domains with $1.17\lambda_0$ and $2.64\lambda_0$ side lengths. The optimization is performed for a material permittivity of $\epsilon_r = 2.26$ ($n = 1.5$). Fig. 23 provides a comparison among these four possible cases. Results indicate that although the topology optimization may reach high efficiencies ($\%90$), the optimization area is obviously a restrictive factor reducing efficiencies to $\%65$ and $\%34$ for $Z = 5$ kΩ and $Z = 20$ kΩ, respectively.

While the results here look promising, it may not be the most optimum with lowest dimensions possible metastructure to provide matching. We were interested to explore fundamental limitations that dimensions of optimization domain impose to the efficiency of the metamaterial. In order to study these limitations, a two dimensional parametric sweep is run on dimensions of the rectangular optimization domain while inverse-design attempts to converge. The procedure is done for load impedances of 50Ω, $5k\Omega$, and $20k\Omega$. Fig. 24 shows results of the study on different dimensions of the optimization domain. The

plots visualize the amount of maximum obtained received power by the LNA for different optimization box sizes. Therefore, we accomplished our initial goal to find a metamaterial topology to minimize reflections from LNA with inverse-designed metamaterials with a comprehensive study on the impact of optimization area dimensions on matching efficiency of the metamaterial for three impedances with distant scales from each other. We explored minimum optimization domain size needed to reach various levels of impedance matching which may come significantly helpful for RF design applications.

CHAPTER A APPENDIX A

A.1 Calculation of the output signal of the full system

Here, we show how to calculate the transmission coefficient of the full (antenna array and waveguide) system. We assume that the incident wave is polarized out of plane (TE polarization) with electric field intensity E_{inc} and incident angle θ. Then, the incident power over a period W is given by

$$P_{\text{inc}} = \frac{|E_{\text{inc}}|^2}{2Z_{\text{TE}}} W, \tag{A.1}$$

where $Z_{\text{TE}} = \eta/\cos\theta$ and $\eta = 120\pi\ \Omega$ is the wave impedance in free space. The collected power at the output channel is found by multiplying the incident power with the receiving efficiency of the antenna array in (2.18) and the transmission coefficient of the differentiating waveguide in (2.44) as

$$P_{\text{out}} = T_{\text{array}} T_{\text{wg}} P_{\text{inc}}. \tag{A.2}$$

Therefore, the total transmission coefficient with respect to power is given by

$$T_{\text{power}} = \frac{P_{\text{out}}}{P_{\text{inc}}} = T_{\text{array}} T_{\text{wg}} \tag{A.3}$$

The output power is also given by

$$P_{\text{out}} = \frac{|E_{\text{out}}|^2}{2Z_{\text{c}}} \int_0^w e^2(x)dx = \frac{|E_{\text{out}}|^2}{4Z_{\text{c}}} w, \tag{A.4}$$

where

$$Z_{\mathrm{c}} = \frac{\eta}{\sqrt{\epsilon_r}\sqrt{1-(f_{\mathrm{c}}/f)^2}} \tag{A.5}$$

is the characteristic impedance of the output channel, $f_{\mathrm{c}} = c/(2w)$ is its cutoff frequency, E_{out} is the electric field intensity at the middle of the channel, $e(x) = \sin(\pi x/w)$ is the electric field profile and w the channel's width. In addition to the power transmission coefficient, we can define a transmission coefficient with respect to the incident and output fields as

$$T_{\mathrm{field}} = \frac{E_{\mathrm{out}}}{E_{\mathrm{inc}}}. \tag{A.6}$$

The magnitude of this transmission coefficient is found by dividing (A.1) and (A.4) as

$$|T_{\mathrm{field}}| = \frac{|E_{\mathrm{out}}|}{|E_{\mathrm{inc}}|} = \sqrt{\frac{P_{\mathrm{out}}}{P_{\mathrm{inc}}}}\sqrt{\frac{2Z_{\mathrm{TE}}}{Z_{\mathrm{c}}}\frac{W}{w}}. \tag{A.7}$$

It is evident that T_{field} and T_{power} are related through

$$|T_{\mathrm{field}}| = \sqrt{T_{\mathrm{power}}}\sqrt{\frac{2Z_{\mathrm{TE}}}{Z_{\mathrm{c}}}\frac{W}{w}}. \tag{A.8}$$

The phase of the transmission coefficient is found by simply subtracting the phases of the output and incident fields. Knowing T, the output signals are calculated as

$$y_n = T_{\mathrm{field}} E_{\mathrm{inc}} e^{-jk_{\mathrm{t}}nW}, \tag{A.9}$$

where $k_{\mathrm{t}} = k\sin\theta$ is the transverse wavenumber of the incident wave, k being the wavenumber in free space.

Assume now that the incident field has a general profile $E_{\text{inc}}(x)$. By using the inverse Fourier transform, we can write

$$E_{\text{inc}}(x) = \frac{1}{2\pi}\int_{-k}^{k} \tilde{E}_{\text{inc}}(k_{\text{t}})e^{-jk_{\text{t}}x}dk_{\text{t}}, \tag{A.10}$$

where

$$\tilde{E}_{\text{inc}}(k_{\text{t}}) = \int_{-\infty}^{\infty} E_{\text{inc}}(x)e^{jk_{\text{t}}x}dx \tag{A.11}$$

is the direct Fourier transform. The limits in (A.10) are from $-k$ to k since the incident field is assumed to be generated by a source at far distance and therefore it does not contain evanescent components. (A.10) indicates that the incident field is a superposition of plane waves with electric field intensities $(1/2\pi)\tilde{E}_{\text{inc}}(k_{\text{t}})$ and wavenumbers k_{t}. Combining this fact with (A.9) leads to

$$y_n = \frac{1}{2\pi}\int_{-k}^{k} T_{\text{field}}(k_{\text{t}})\tilde{E}_{\text{inc}}(k_{\text{t}})e^{-jk_{\text{t}}nW}dk_{\text{t}}. \tag{A.12}$$

(A.12) is the one used to derive the results in Fig. 5 of the main text.

A.2 Lens Antenna Design

Utilizing the Fermat's principle, one can easily show that a dielectric elliptical lens with a proper eccentricity collimates illuminating plane waves into the focus point of the ellipse. Fig. 25 shows the design evolution of a lens of this kind. Having experimental limitations in mind, the elliptical lens is usually replaced with an extended hemispherical lens, as in Fig. 26 [30]. A quarter-wevelength coating layer is also essential to minimize reflections.

An air-filled leaky-wave cavity is also added between the extended hemispherical lens

and the feed to confine the feed's radiation pattern into the hemispherical part of the lens and avoid spill-over losses [31]. The leaky-wave cavity also helps with impedance matching between the feed and the lens. In order to achieve a directive beam in the broadside direction, the height of the leaky-wave cavity should approximately be half a wavelength. The beamwidth of the leaky-wave cavity's radiation pattern is determined by

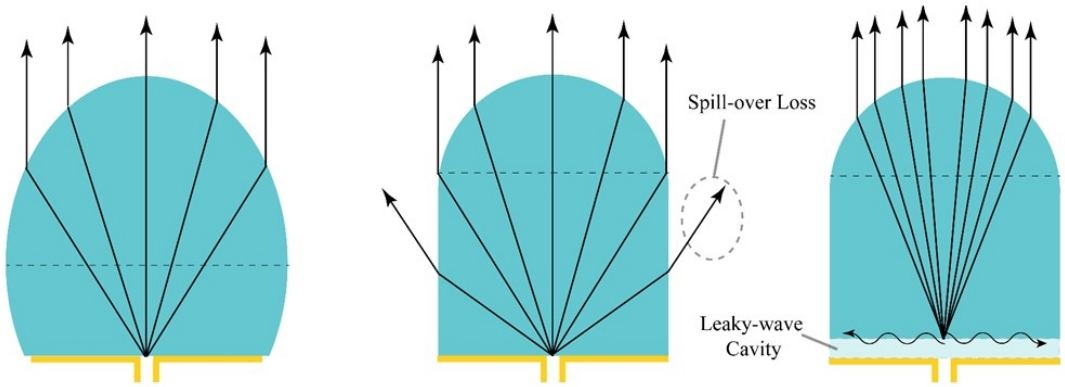

Figure 25: Left, middle and right lenses show ellptical configuration derived from Fermat's law, trancated lens and leaky-wave cavity embedded lens, respectively.

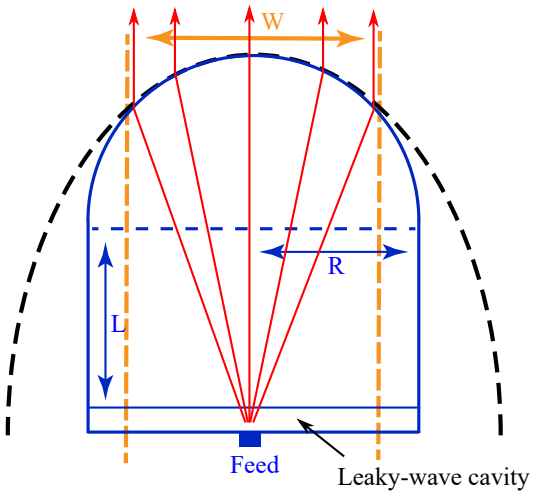

Figure 26: Lens design illustration. The dotted black and solid blue lines show the elliptical and extended hemispherical lenses, respectively. The orange dashed lines indicated the truncated region for the case of a periodic array. The solid red lines depict the radiated field.

the contrast between the lens's and cavity's permittivities. For example, for the parameters used in the paper, the beamwidth of the leaky-wave cavity is approximately 24°. Therefore, in order to achieve alignment between the hemispherical lens and the leaky-wave cavity's beam, it might be necessary to adjust the height L of the region between the lens and the cavity.

For the case of an antenna array, it might be necessary to truncate the lens along the horizontal direction by a distance equal to the distance between the array's antennas. In this case, the leaky-wave cavity should create a beam that fits within the truncated part of the lens (between the orange dashed lines in Fig. 26). For the material parameters and the periodicity used in our analysis, we found through numerical optimization with respect to R and L that the best response is achieved for $R = 2.111W$ and $L = 0.02R$. These parameters lead to a broadside gain of 14.2 dB, which is fairly close to the optimum value of 17.7 dB from (2.22).

CHAPTER B APPENDIX B

B.1 Wavelet transform matrix

In signal processing the discrete wavelet transform (DWT) is defined through a series of successive low- and high-pass filtering operations, followed by down-sampling operations. If this process is applied P times, the DWT is said to have a scale P. Assuming a one-dimensional discrete signal x_n of length $N = 2^J$, this procedure is mathematically expressed through the relations [62]

$$S_{j+1,n} = \frac{1}{\sqrt{2}} \sum_{m=0}^{2^{J-j}-1} c_{m-2n} S_{j,m}, \tag{B.1}$$

$$T_{j+1,n} = \frac{1}{\sqrt{2}} \sum_{m=0}^{2^{J-j}-1} b_{m-2n} S_{j,m}, \tag{B.2}$$

with $S_{0,n} = x_n$, and c_n and b_n the so-called *scaling* and *wavelet* coefficients associated with a low-pass and a high-pass filtering operation, respectively. Eq. (B.1) and (B.2) are recursively applied from $j = 0$ to $j = P - 1$. The output of the transform consists of the coefficients $S_{P,n}$, with $0 \leq n < 2^{J-P}$, and $T_{j,n}$, with $1 \leq j \leq P$ and $0 \leq n < 2^{J-j}$, and is of the same size as the input vector. The DWT coefficients also satisfy the equation [62]

$$\sum_{n=0}^{2^J-1} x_n \phi_{0,n}(x) = \sum_{n=0}^{2^{J-P}-1} S_{P,n} \phi_{P,n}(x) + \sum_{j=1}^{P} \sum_{n=0}^{2^{J-j}-1} T_{j,n} \psi_{m,n}(x), \tag{B.3}$$

where $\phi_{j,n}(t)$ and $\psi_{j,n}(t)$ are the scaling and wavelet functions, respectively, of scale j and translation parameter n. The scaling and wavelet functions in the right side of Eq. (B.3) form an orthonormal set, allowing us to take the inner product of Eq. (B.3) with each of

these functions and find the DWT coefficients as

$$S_{P,n} = \sum_{m=0}^{2^J-1} (\phi_{P,n}, \phi_{0,m}) x_m, \tag{B.4}$$

$$T_{j,n} = \sum_{m=0}^{2^J-1} (\psi_{j,n}, \phi_{0,m}) x_m, \tag{B.5}$$

where $(\phi, \psi) = \int_{-\infty}^{\infty} \phi(x)\psi(x)dx$. The DTW coefficients can be ordered in the output vector in any way. Here, we choose to order them as

$$\mathbf{y} = \begin{bmatrix} \mathbf{y}_0 \\ \mathbf{y}_1 \\ \vdots \\ \mathbf{y}_{2^{N-M}-1} \end{bmatrix}, \tag{B.6}$$

where $\mathbf{y}_i$ are vectors of length 2^P defined as

$$\begin{aligned} \mathbf{y}_0 &= [\ S_{P,0}\ \ T_{P,0}\ \ T_{P-1,0}\ \ T_{P-1,1}\ \ T_{P-2,0}\ \ \dots\ \ T_{P-2,3}\ \ \dots\ ]^{\mathrm{T}} \\ \mathbf{y}_1 &= [\ S_{P,1}\ \ T_{P,1}\ \ T_{P-1,2}\ \ T_{P-1,3}\ \ T_{P-2,4}\ \ \dots\ \ T_{P-2,7}\ \ \dots\ ]^{\mathrm{T}} \\ \mathbf{y}_2 &= [\ S_{P,2}\ \ T_{P,2}\ \ T_{P-1,4}\ \ T_{P-1,5}\ \ T_{P-2,8}\ \ \dots\ \ T_{P-2,11}\ \ \dots\ ]^{\mathrm{T}} \\ &\ \ \vdots \end{aligned}. \tag{B.7}$$

From these definitions and Eqs. (B.4) and (B.5) we find

$$\mathbf{y}_i = \sum_{j=0}^{2^{J-P}-1} \mathbf{H}_{ij}\mathbf{x}_j, \tag{B.8}$$

where

$$\begin{aligned}
\mathbf{x}_0 &= \begin{bmatrix} x_0 & x_1 & x_2 & \dots & x_{2^P-1} \end{bmatrix}^{\mathrm{T}} \\
\mathbf{x}_1 &= \begin{bmatrix} x_{2^P} & x_{2^P+1} & x_{2^P+2} & \dots & x_{2^{P+1}-1} \end{bmatrix}^{\mathrm{T}} \\
\mathbf{x}_2 &= \begin{bmatrix} x_{2^{P+1}} & x_{2^{P+1}+1} & x_{2^{P+1}+2} & \dots & x_{2^{P+1}-1} \end{bmatrix}^{\mathrm{T}} \\
&\vdots
\end{aligned}. \tag{B.9}$$

and

$$\mathbf{H}_{ij} = \begin{bmatrix} (\phi_{P,i}, \phi_{0,j2^P}) & (\phi_{P,i}, \phi_{0,j2^P+1}) & (\phi_{P,i}, \phi_{0,j2^P+2}) & \dots \\ (\psi_{P,i}, \phi_{0,j2^P}) & (\psi_{P,i}, \phi_{0,j2^P+1}) & (\psi_{P,i}, \phi_{0,j2^P+2}) & \dots \\ (\psi_{P-1,i2}, \phi_{0,j2^P}) & (\psi_{P-1,i2}, \phi_{0,j2^P+1}) & (\psi_{P-1,i2}, \phi_{0,j2^P+2}) & \dots \\ (\psi_{P-1,i2+1}, \phi_{0,j2^P}) & (\psi_{P-1,i2+1}, \phi_{0,j2^P+1}) & (\psi_{P-1,i2+1}, \phi_{0,j2^P+2}) & \dots \\ \vdots & \vdots & \vdots & \ddots \end{bmatrix}. \tag{B.10}$$

From the translation and scaling properties of the scaling and wavelet functions we know

$$\phi_{j,n}(x) = 2^{-j/2}\phi(2^{-j}x - n), \tag{B.11}$$

$$\psi_{j,n}(x) = 2^{-j/2}\psi(2^{-j}x - n), \tag{B.12}$$

where $\phi(x)$ and $\psi(x)$ are the mother scaling and wavelet functions, respectively. Then, it follows

$$\phi_{P,i}(x) = \phi_{P,0}\big(x - i2^P\big) \tag{B.13}$$

and

$$(\phi_{P,i}, \phi_{0,j2^P+n}) = \Big(\phi_{P,0}\big(x - i2^P\big), \phi_{0,j2^P+n}(x)\Big) \tag{B.14}$$

$$= \Big(\phi_{P,0}(x), \phi_{0,j2^P+n}\big(x + i2^P\big)\Big)$$

$$= (\phi_{P,0}, \phi_{0,(j-i)2^P+n}). \tag{B.15}$$

Furthermore, if $k \leq P$,

$$\psi_{k,i2^{P-k}+n}(x) = \psi_{k,n}\big(x - i2^P\big) \tag{B.16}$$

and

$$(\psi_{k,i2^{P-k}+n}, \phi_{0,j2^P}) = \Big(\psi_{k,n}\big(x - i2^P\big), \phi_{0,j2^P}(x)\Big) \tag{B.17}$$

$$= \Big(\psi_{k,n}(x), \phi_{0,j2^P}\big(x + i2^P\big)\Big)$$

$$= \big(\psi_{k,n}, \phi_{0,(j-i)2^P}\big). \tag{B.18}$$

Applying Eqs. (B.15) and (B.18) on Eq. (B.10) gives $\mathbf{H}_{ij} = \mathbf{H}_{0,j-i}$, Then, Eq. (B.8) can be written as

$$\mathbf{y}_i = \sum_{j=0}^{2^{J-P}-1} \mathbf{H}_{j-i}\mathbf{x}_j, \tag{B.19}$$

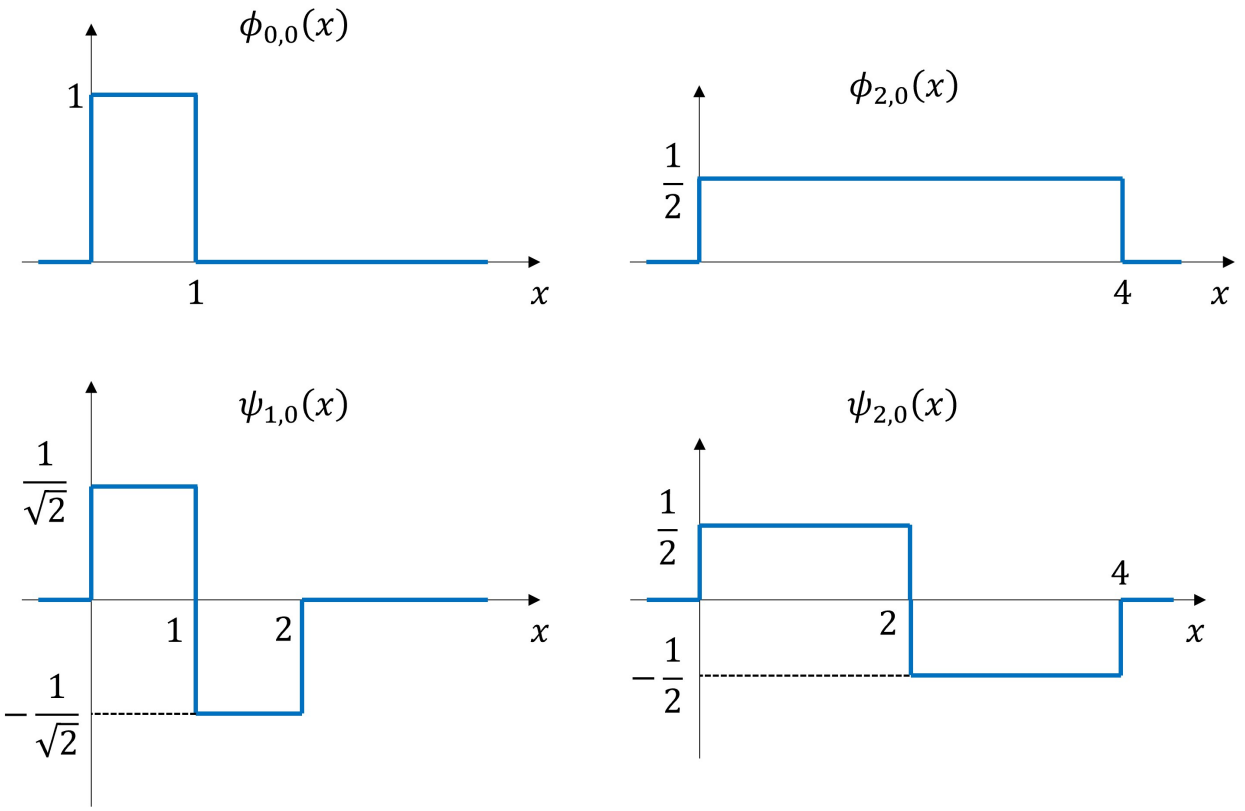

Figure 27: Scaling and wavelet functions of the Haar transform for scales 0 to 2.

where $\mathbf{H}_i \equiv \mathbf{H}_{0,i}$. We conclude that the DWT can be expressed in the block-matrix form

$$\begin{bmatrix} \mathbf{y}_0 \\ \mathbf{y}_1 \\ \mathbf{y}_2 \\ \vdots \end{bmatrix} = \begin{bmatrix} \mathbf{H}_0 & \mathbf{H}_1 & \mathbf{H}_2 & \dots \\ \mathbf{H}_{-1} & \mathbf{H}_0 & \mathbf{H}_1 & \dots \\ \mathbf{H}_{-2} & \mathbf{H}_{-1} & \mathbf{H}_0 & \dots \\ \vdots & \vdots & \vdots & \ddots \end{bmatrix} \begin{bmatrix} \mathbf{x}_0 \\ \mathbf{x}_1 \\ \mathbf{x}_2 \\ \vdots \end{bmatrix}. \tag{B.20}$$

For the Haar wavelet transform the mother scaling and wavelet functions are given by

$$\phi(x) = \begin{cases} 1, & 0 \leq x < 1, \\ 0, & \text{elsewhere} \end{cases}, \tag{B.21}$$

$$\psi(x) = \begin{cases} 1, & 0 \leq x < 0.5, \\ -1, & 0.5 \leq x < 1, \\ 0, & \text{elsewhere} \end{cases}. \tag{B.22}$$

The scaling and wavelet functions for scales 0 to 2 and zero translation are depicted in Fig. 27. For a transform of scale $P = 2$ the elements of the transform's block matrix are given by

$$\mathbf{H}_i = \begin{bmatrix} (\phi_{2,0}, \phi_{0,4i}) & (\phi_{2,0}, \phi_{0,4i+1}) & (\phi_{2,0}, \phi_{0,4i+2}) & (\phi_{2,0}, \phi_{0,4i+3}) \\ (\psi_{2,0}, \phi_{0,4i}) & (\psi_{2,0}, \phi_{0,4i+1}) & (\psi_{2,0}, \phi_{0,4i+2}) & (\psi_{2,0}, \phi_{0,4i+3}) \\ (\psi_{1,0}, \phi_{0,4i}) & (\psi_{1,0}, \phi_{0,4i+1}) & (\psi_{1,0}, \phi_{0,4i+2}) & (\psi_{1,0}, \phi_{0,4i+3}) \\ (\psi_{1,1}, \phi_{0,4i}) & (\psi_{1,1}, \phi_{0,4i+1}) & (\psi_{1,1}, \phi_{0,4i+2}) & (\psi_{1,1}, \phi_{0,4i+3}) \end{bmatrix}. \tag{B.23}$$

By replacing into this equation the scaling and wavelet functions of Fig. 27 we find

$$\mathbf{H}_0 = \frac{1}{2} \begin{bmatrix} 1 & 1 & 1 & 1 \\ 1 & 1 & -1 & -1 \\ \sqrt{2} & -\sqrt{2} & 0 & 0 \\ 0 & 0 & \sqrt{2} & -\sqrt{2} \end{bmatrix}. \tag{B.24}$$

Furthermore, since $\phi_{0,0}(x)$, $\psi_{2,0}(t)$, $\psi_{1,0}(x)$ and $\psi_{0,1}(x)$ have a limited support between 0 and 4, they have zero overlap with $\phi_{0,4i}(x)$, $\phi_{0,4i+1}(x)$, $\phi_{0,4i+2}(x)$ and $\phi_{0,4i+3}(x)$ for $i \neq 0$,

resulting in $\mathbf{H}_i = \mathbf{0}$ for $i \neq 0$. Although shown here for a transform of scale 2, this fact applies to any scale P.

B.2 Output signals of the lenses

Consider a lens as in Fig. 28 converting an incident beam to a waveguide mode. The electric field is assumed to be polarized parallel to the z-axis. The lens is designed to perfectly convert an incident beam on its front face S_1 with a real-valued profile $W(x)$ for the electric field to a waveguide mode with electric field $x_0 e_0(x)$, where $e_0(x)$ is the modal field and x_0 its amplitude. The incident beam is assumed to have unitary power, i.e.,

$$\int \frac{W^2(x)}{2\eta_0} dx = 1. \tag{B.25}$$

Furthermore, the mode field is selected such that $|x_0|^2$ is equal to the power, which requires [64]

$$\frac{\beta}{2\omega\mu_0} \int [e_0(x)]^2 dx = 1, \tag{B.26}$$

where β is the modal wavenumber. Power conservation requires $|x_0| = 1$. The phase of x_0 can be cancelled through appropriate selection of the reference plane of the waveguide port, so from now on we take $x_0 = 1$. From time reversal it follows that applying an input field $e_0(x)$ to the waveguide port results in a wave with profile $W(x)$ at the front face of the lens.

Now consider excitation of the lens with an incident wave with profile $E_{\text{inc}}(x)$ at its front face. To find the output signal at the waveguide we apply the Lorentz reciprocity

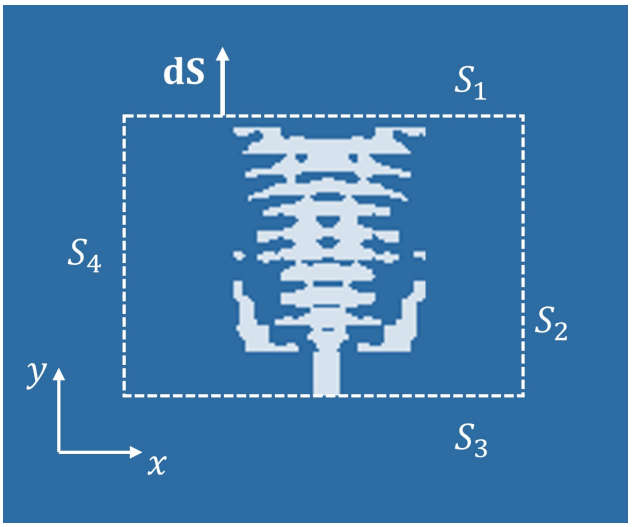

Figure 28: Contour around a lens for the application of the reciprocity theorem.

theorem on the volume defined by S_1–S_4 in Fig. 28. Specifically, we have [64]

$$\oint_S (\mathbf{E}^a \times \mathbf{H}^b - \mathbf{E}^b \times \mathbf{H}^a) \cdot \mathbf{dS} = 0, \tag{B.27}$$

where $\mathbf{E}^a$, $\mathbf{H}^a$ and $\mathbf{E}^b$, $\mathbf{H}^b$ are two pairs of electric and magnetic fields that satisfy Maxwell equations. Let the a-indexed fields be those associated with the incident wave and the b-index fields be the fields for excitation from the waveguide port with a mode of unitary amplitude. Since S_2 and S_4 can be taken arbitrarily far from the structure, their contribution in the integral can be neglected. On S_1 the electric fields are $\mathbf{E}^a(x) = E_{\text{inc}}(x)\hat{\mathbf{z}}$ and $\mathbf{E}^b(x) = W(x)\hat{\mathbf{z}}$. A rigorous computation of the magnetic fields would have been based on Faraday's law. However, if the variation of the electric field is much slower than the

wavelength, we can approximate the magnetic fields as

$$\mathbf{H}^a(x) \approx \frac{(-\hat{\mathbf{y}}) \times \mathbf{E}^a(x)}{\eta_0} = -\frac{E_{\text{inc}}(x)}{\eta_0}\hat{\mathbf{x}}, \tag{B.28}$$

$$\mathbf{H}^b(x) \approx \frac{\hat{\mathbf{y}} \times \mathbf{E}^b(x)}{\eta_0} = \frac{W(x)}{\eta_0}\hat{\mathbf{x}}. \tag{B.29}$$

Then, the integral on S_1 is written as

$$\int_{S_1} (\mathbf{E}^a \times \mathbf{H}^b - \mathbf{E}^b \times \mathbf{H}^a) \cdot \mathbf{dS} = \frac{2}{\eta_0} \int E_{\text{inc}}(x) W(x) dx. \tag{B.30}$$

On S_2 the electric fields are $\mathbf{E}^a(x) = xe_0(x)\hat{\mathbf{z}}$ and $\mathbf{E}^b(x) = e_0(x)\hat{\mathbf{z}}$, where x is the signal at the waveguide port due to the incident wave $E_{\text{inc}}(x)$. To determine the transverse component of the magnetic field we invoke Faraday's law with $e^{\pm j\beta y}$ for the field dependence along the y-axis, from which we find

$$H_x(x) = \pm\frac{\beta}{\omega\mu_0} E_z(x), \tag{B.31}$$

with the positive and negative signs holding for modes propagating parallel to the positive and negative y-axis, respectively. It follows

$$H_x^a(x) = -\frac{\beta}{\omega\mu_0} xe_0(x) \tag{B.32}$$

$$H_x^b(x) = \frac{\beta}{\omega\mu_0} e_0(x). \tag{B.33}$$

Then, the integral on S_2 is found

$$\int_{S_2} (\mathbf{E}^a \times \mathbf{H}^b - \mathbf{E}^b \times \mathbf{H}^a) \cdot \mathbf{dS} = -x \frac{2\beta}{\omega\mu_0} \int [e_0(x)]^2 dx. \tag{B.34}$$

Replacing Eqs. (B.30) and (B.34) into Eq. (B.27) and using Eq. (B.26) yields

$$x = \frac{1}{2\eta_0} \int E_{\text{inc}}(x) W(x) dx. \tag{B.35}$$

Dividing this equation with Eq. (B.25) gives

$$x = \frac{\int E_{\text{inc}}(x) W(x) dx}{\int [W(x)]^2 dx}. \tag{B.36}$$

REFERENCES

[1] A. Silva, F. Monticone, G. Castaldi, V. Galdi, A. Alù, and N. Engheta, "Performing mathematical operations with metamaterials," *Science*, vol. 343, no. January, pp. 160–164, 2014.

[2] R. Athale and D. Psaltis, "Optical Computing: Past and Future," *Opt. Photonics News*, vol. 27, no. 6, pp. 32–39, 2016.

[3] D. R. Solli and B. Jalali, "Analog optical computing," *Nat. Photon.*, vol. 9, no. 11, pp. 704–706, 2015.

[4] A. Pors, M. G. Nielsen, and S. I. Bozhevolnyi, "Analog Computing Using Reflective Plasmonic Metasurfaces," *Nano Lett.*, vol. 15, pp. 791–797, 2015.

[5] A. Youssefi, F. Zangeneh-Nejad, S. Abdollahramezani, and A. Khavasi, "Analog computing by Brewster effect," *Opt. Lett.*, vol. 41, no. 15, pp. 3467–3470, 2016.

[6] W. Wu, W. Jiang, J. Yang, S. Gong, and Y. Ma, "Multilayered analog optical differentiating device: performance analysis on structural parameters," *Opt. Lett.*, vol. 42, no. 24, pp. 5270–5273, 2017.

[7] T. Zhu, Y. Zhou, Y. Lou, H. Ye, M. Qiu, Z. Ruan, and S. Fan, "Plasmonic computing of spatial differentiation," *Nat. Commun.*, vol. 8, no. May, p. 15391, 2017.

[8] C. Guo, M. Xiao, M. Minkov, Y. Shi, and S. Fan, "Photonic crystal slab Laplace operator for image differentiation," *Optica*, vol. 5, no. 3, p. 251, 2018.

[9] H. Kwon, D. Sounas, A. Cordaro, A. Polman, and A. Alù, "Nonlocal Metasurfaces for Optical Signal Processing," *Phys. Rev. Lett.*, vol. 121, no. 17, p. 173004, 2018.

[10] Y. Hwang, T. J. Davis, J. Lin, and X.-C. Yuan, "Plasmonic circuit for second-order spa-

tial differentiation at the subwavelength scale," *Opt. Express*, vol. 26, no. 6, pp. 7368–7375, 2018.

[11] D. A. Bykov, L. L. Doskolovich, A. A. Morozov, V. V. Podlipnov, E. A. Bezus, P. Verma, and V. A. Soifer, "First-order optical spatial differentiator based on a guided-mode resonant grating," *Opt. Express*, vol. 26, no. 8, pp. 10997–11006, 2018.

[12] T. Zhu, Y. Lou, Y. Zhou, J. Zhang, J. Huang, Y. Li, H. Luo, S. Wen, S. Zhu, Q. Gong, M. Qiu, and Z. Ruan, "Generalized Spatial Differentiation from the Spin Hall Effect of Light and Its Application in Image Processing of Edge Detection," *Phys. Rev. Appl.*, vol. 11, p. 034043, 2019.

[13] T. J. Davis, F. Eftekhari, D. E. Gómez, and A. Roberts, "Metasurfaces with Asymmetric Optical Transfer Functions for Optical Signal Processing," *Phys. Rev. Lett.*, vol. 123, p. 013901, 2019.

[14] J. Zhou, H. Qian, C.-f. Chen, J. Zhao, G. Li, Q. Wu, H. Luo, S. Wen, and Z. Liu, "Optical edge detection based on high-efficiency dielectric metasurface," *Proc. Natl. Acad. Sci.*, vol. 116, no. 23, pp. 11137–11140, 2019.

[15] A. Cordaro, H. Kwon, D. Sounas, A. F. Koenderink, A. Alù, and A. Polman, "High-Index Dielectric Metasurfaces Performing Mathematical Operations," *Nano Lett.*, vol. 19, no. 12, pp. 8418–8423, 2019.

[16] Y. Zhou, H. Zheng, I. I. Kravchenko, and J. Valentine, "Flat optics for image differentiation," *Nat. Photon.*, vol. 14, pp. 316–323, 2020.

[17] Y. Zhou, W. Wu, R. Chen, W. Chen, R. Chen, and Y. Ma, "Analog Optical Spatial Differentiators Based on Dielectric Metasurfaces," *Adv. Opt. Mater.*, vol. 8, p. 1901523, 2020.

[18] A. Marandi, Z. Wang, K. Takata, R. L. Byer, and Y. Yamamoto, "Network of time-multiplexed optical parametric oscillators as a coherent Ising machine," *Nat. Photon.*, vol. 8, no. 12, pp. 937–942, 2014.

[19] H. Takesue, O. Tadanaga, Y. Haribara, K. Enbutsu, T. Sonobe, P. L. McMahon, K. Inoue, S. Tamate, A. Marandi, T. Honjo, K. Igarashi, H. Takenouchi, S. Utsunomiya, K.-i. Kawarabayashi, T. Umeki, K. Aihara, and T. Inagaki, "A coherent Ising machine for 2000-node optimization problems," *Science*, vol. 354, no. 6312, pp. 603–606, 2016.

[20] Y. Shen, N. C. Harris, S. Skirlo, M. Prabhu, T. Baehr-Jones, M. Hochberg, X. Sun, S. Zhao, H. Larochelle, D. Englund, and M. Soljačić, "Deep learning with coherent nanophotonic circuits," *Nat. Photon.*, vol. 11, pp. 441–446, jun 2017.

[21] R. Hamerly, L. Bernstein, A. Sludds, M. Soljačić, and D. Englund, "Large-Scale Optical Neural Networks Based on Photoelectric Multiplication," *Phys. Rev. X*, vol. 9, no. 2, p. 021032, 2019.

[22] X. Lin, Y. Rivenson, N. T. Yardimci, M. Veli, Y. Luo, M. Jarrahi, and A. Ozcan, "All-optical machine learning using diffractive deep neural networks," *Science*, vol. 361, no. 6406, pp. 1004–1008, 2018.

[23] T. W. Hughes, I. A. Williamson, M. Minkov, and S. Fan, "Wave physics as an analog recurrent neural network," *Sci. Adv.*, vol. 5, no. 12, p. eaay6946, 2019.

[24] N. M. Estakhri, B. Edwards, and N. Engheta, "Inverse-designed metastructures that solve equations," *Science*, vol. 363, pp. 1333–1338, 2019.

[25] F. Zangeneh-Nejad and R. Fleury, "Topological analog signal processing," *Nat. Commun.*, vol. 10, p. 2058, 2019.

[26] H. Stark, *Application of Optical Fourier Transforms*. N.Y.: Academic Press Inc., 1982.

[27] A. Antoniou, *Digital Filters: Analysis, Design, and Signal Processing Applications*. McGraw-Hill Education, 2018.

[28] S. Molesky, Z. Lin, A. Y. Piggott, W. Jin, J. Vucković, and A. W. Rodriguez, "Inverse design in nanophotonics," *Nat. Photon.*, vol. 12, no. 11, pp. 659–670, 2018.

[29] C. A. Balanis, *Antenna Theory: Analysis and Design*. Hoboken, N.J.: John Wiley & Sons, Inc., 2005.

[30] D. F. Filipovic, S. S. Gearhart, and G. M. Rebeiz, "Double-slot antennas on extended hemispherical and elliptical silicon dielectric lenses," *IEEE Trans. Microwav. Theory Techn.*, vol. 41, no. 10, pp. 1738–1749, 1993.

[31] A. Neto, "UWB, Non Dispersive Radiation From the Planarly Fed Leaky Lens Antenna— Part 1: Theory and Design," *IEEE Trans. Antennas Propag.*, vol. 58, no. 7, pp. 2238–2247, 2010.

[32] A. Neto, S. Monni, and F. Nennie, "UWB, Non Dispersive Radiation From the Planarly Fed Leaky Lens Antenna—Part II: Demonstrators and Measurements," *IEEE Trans. Antennas Propag.*, vol. 58, no. 7, pp. 2248–2258, 2010.

[33] C. A. Balanis, *Antenna theory: analysis and design*. John wiley & sons, 2016.

[34] G. B. Arfken and H. J. Weber, *Mathematical methods for physicists*. American Association of Physics Teachers, 1999.

[35] Songnan Yang and A. E. Fathy, "Synthesis of a compound T-junction for a two-way splitter with arbitrary power ratio," in *IEEE MTT-S International Microwave Symposium Digest, 2005.*, pp. 4 pp.–, 2005.

[36] J. W. Goodman, A. Dias, and L. Woody, "Fully parallel, high-speed incoherent optical method for performing discrete fourier transforms," *Optics Letters*, vol. 2, no. 1, pp. 1–3, 1978.

[37] J. W. Goodman and M. S. Song, "Performance limitations of an analog method for solving simultaneous linear equations," *Applied Optics*, vol. 21, no. 3, pp. 502–506, 1982.

[38] D. Psaltis, "Two-dimensional optical processing using one-dimensional input devices," *Proceedings of the IEEE*, vol. 72, no. 7, pp. 962–974, 1984.

[39] T. Inagaki, Y. Haribara, K. Igarashi, T. Sonobe, S. Tamate, T. Honjo, A. Marandi, P. L. McMahon, T. Umeki, K. Enbutsu, *et al.*, "A coherent ising machine for 2000-node optimization problems," *Science*, vol. 354, no. 6312, pp. 603–606, 2016.

[40] A. Youssefi, F. Zangeneh-Nejad, S. Abdollahramezani, and A. Khavasi, "Analog computing by brewster effect," *Optics letters*, vol. 41, no. 15, pp. 3467–3470, 2016.

[41] Y. Shen, N. C. Harris, S. Skirlo, M. Prabhu, T. Baehr-Jones, M. Hochberg, X. Sun, S. Zhao, H. Larochelle, D. Englund, *et al.*, "Deep learning with coherent nanophotonic circuits," *Nature Photonics*, vol. 11, no. 7, pp. 441–446, 2017.

[42] T. Zhu, Y. Zhou, Y. Lou, H. Ye, M. Qiu, Z. Ruan, and S. Fan, "Plasmonic computing of spatial differentiation," *Nature communications*, vol. 8, no. 1, pp. 1–6, 2017.

[43] C. Guo, M. Xiao, M. Minkov, Y. Shi, and S. Fan, "Photonic crystal slab laplace operator for image differentiation," *Optica*, vol. 5, no. 3, pp. 251–256, 2018.

[44] X. Lin, Y. Rivenson, N. T. Yardimci, M. Veli, Y. Luo, M. Jarrahi, and A. Ozcan, "All-optical machine learning using diffractive deep neural networks," *Science*, vol. 361, no. 6406, pp. 1004–1008, 2018.

[45] H. Kwon, D. Sounas, A. Cordaro, A. Polman, and A. Alù, "Nonlocal metasurfaces for optical signal processing," *Physical Review Letters*, vol. 121, no. 17, p. 173004, 2018.

[46] P. del Hougne and G. Lerosey, "Leveraging chaos for wave-based analog computation: Demonstration with indoor wireless communication signals," *Physical Review X*, vol. 8, no. 4, p. 041037, 2018.

[47] N. Mohammadi Estakhri, B. Edwards, and N. Engheta, "Inverse-designed metastructures that solve equations," *Science*, vol. 363, no. 6433, pp. 1333–1338, 2019.

[48] F. Zangeneh-Nejad and R. Fleury, "Topological analog signal processing," *Nature Communications*, vol. 10, no. 1, pp. 1–10, 2019.

[49] J. Zhou, H. Qian, C.-F. Chen, J. Zhao, G. Li, Q. Wu, H. Luo, S. Wen, and Z. Liu, "Optical edge detection based on high-efficiency dielectric metasurface," *Proceedings of the National Academy of Sciences*, vol. 116, no. 23, pp. 11137–11140, 2019.

[50] M. W. Matthès, P. del Hougne, J. de Rosny, G. Lerosey, and S. M. Popoff, "Optical complex media as universal reconfigurable linear operators," *Optica*, vol. 6, no. 4, pp. 465–472, 2019.

[51] T. W. Hughes, I. A. Williamson, M. Minkov, and S. Fan, "Wave physics as an analog recurrent neural network," *Science advances*, vol. 5, no. 12, p. eaay6946, 2019.

[52] T. Yan, J. Wu, T. Zhou, H. Xie, F. Xu, J. Fan, L. Fang, X. Lin, and Q. Dai, "Fourier-space diffractive deep neural network," *Physical review letters*, vol. 123, no. 2, p. 023901, 2019.

[53] G. Wetzstein, A. Ozcan, S. Gigan, S. Fan, D. Englund, M. Soljačić, C. Denz, D. A. Miller, and D. Psaltis, "Inference in artificial intelligence with deep optics and photonics," *Nature*, vol. 588, no. 7836, pp. 39–47, 2020.

[54] Y. Zhou, H. Zheng, I. I. Kravchenko, and J. Valentine, "Flat optics for image differentiation," *Nature Photonics*, vol. 14, no. 5, pp. 316–323, 2020.

[55] O. Kulce, D. Mengu, Y. Rivenson, and A. Ozcan, "All-optical synthesis of an arbitrary linear transformation using diffractive surfaces," *Light: Science & Applications*, vol. 10, no. 1, pp. 1–21, 2021.

[56] P. Camayd-Muñoz, C. Ballew, G. Roberts, and A. Faraon, "Multifunctional volumetric meta-optics for color and polarization image sensors," *Optica*, vol. 7, no. 4, pp. 280–283, 2020.

[57] F. Zangeneh-Nejad, D. L. Sounas, A. Alù, and R. Fleury, "Analogue computing with metamaterials," *Nature Reviews Materials*, vol. 6, no. 3, pp. 207–225, 2021.

[58] R. Hamerly, "The future of deep learning is photonic: reducing the energy needs of neural networks might require computing with light," *IEEE Spectrum*, vol. 58, no. 7, pp. 30–47, 2021.

[59] D. A. Miller, "Self-configuring universal linear optical component," *Photonics Research*, vol. 1, no. 1, pp. 1–15, 2013.

[60] A. Momeni, H. Rajabalipanah, A. Abdolali, and K. Achouri, "Generalized optical signal processing based on multioperator metasurfaces synthesized by susceptibility tensors," *Physical Review Applied*, vol. 11, no. 6, p. 064042, 2019.

[61] R. C. Gonzalez and R. E. Woods, *Digital image processing*. Upper Saddle River, N.J.: Prentice Hall, 2002.

[62] P. S. Addison, *The Illustrated Wavelet Transform Handbook Introductory Theory and Applications in Science, Engineering, Medicine and Finance*. CRC Press, 2002.

[63] A. Y. Piggott, J. Lu, K. G. Lagoudakis, J. Petykiewicz, T. M. Babinec, and J. Vučković, "Inverse design and demonstration of a compact and broadband on-chip wavelength demultiplexer," *Nature Photonics*, vol. 9, no. 6, pp. 374–377, 2015.

[64] H. A. Haus, *Waves and Fields in Optoelectronics*. Englewood Cliffs, NJ: Prentice Hall, 1984.

ABSTRACT

OPTICAL SIGNAL PROCESSING WITH DISCRETE-SPACE METAMATERIALS

by

MOHAMMAD MOEIN MOEINI

August 2022

Advisor: Prof. Dimitrios L. Sounas

Major: Electrical Engineering

Degree: Doctor of Philosophy

As digital circuits are approaching the limits of Moore's law, a great deal of effort has been directed to alternative computing approaches. Among them, the old concept of optical signal processing (OSP) has attracted attention, revisited in the light of metamaterials and nano-photonics. This approach has been successful in realizing basic mathematical operations, such as derivatives and integrals, but it is difficult to be applied to more complex ones. Inspired by digital filters, we propose a radically new OSP approach, able to realize arbitrary mathematical operations over a nano-photonic platform. We demonstrate this concept for the case of spatial differentiation, image compression and color encoding through a heuristic design based on a waveguide with periodic arrays of input/output channels at its opposite walls.

AUTOBIOGRAPHICAL STATEMENT

Publications

- Mohammad Moein Moeini, and Dimitrios L. Sounas. "Discrete space optical signal processing." Optica 7.10 (2020)
- Mohammad Moein Moeini, and Dimitrios L. Sounas. "Topology-Optimized Metamaterials for Optical Signal Compression." 2021 Fifteenth International Congress on Artificial Materials for Novel Wave Phenomena (Metamaterials). IEEE, 2021.
- Dimitrios L. Sounas, and Mohammad Moein Moeini. "Analog Signal Processing with Discrete Space Metamaterials." 2021 International Applied Computational Electromagnetics Society Symposium (ACES). IEEE, 2021.
- Mohammad Moein Moeini, and Dimitrios L. Sounas. "Image Compression with Light" (under review)
- Mohammad Moein Moeini, and Dimitrios L. Sounas. "Wave-based Color Encoding" (in preparation)
- Mohammad Moein Moeini, and Dimitrios L. Sounas. "Inverse-designed High Impedance Matching Metamaterials" (in preparation)

Education

- PhD in Electrical Engineering, Wayne State University, USA , 2022.
- M.Sc in Electrical Engineering, Iran University of Science and Technology, Iran, 2019.
- B.Sc in Biomedical Engineering, Hamedan University of Technology, Iran, 2016.